Chemical analysis of the Asian Tropopause Aerosol Layer (ATAL) with emphasis on secondary aerosol particles using aircraft based in situ aerosol mass spectrometry

Oliver Appel[1,2], Franziska Köllner[2], Antonis Dragoneas[1,2], Andreas Hünig[1,2], Sergej Molleker[1], Hans Schlager[3], Christoph Mahnke[1,4], Ralf Weigel[2], Max Port[2,5], Christiane Schulz[1,6], Frank Drewnick[1], Bärbel Vogel[7], Fred Stroh[7], and Stephan Borrmann[1,2]

[1]Max Planck Institute for Chemistry, Mainz, Germany
[2]Institute for Atmospheric Physics, Johannes Gutenberg University, Mainz, Germany
[3]Deutsches Zentrum für Luft- und Raumfahrt (DLR), Institut für Physik der Atmosphäre, Oberpfaffenhofen, Germany
[4]now at: Institute of Energy and Climate Research (IEK-8), Forschungszentrum Jülich GmbH, Jülich, Germany
[5]now at: Montessori Zentrum Hofheim, Germany
[6]now at: Leibniz-Zentrum für Agrarlandschaftsforschung, Müncheberg, Germany
[7]Institute of Energy and Climate Research (IEK-7), Forschungszentrum Jülich, Jülich, Germany

Correspondence: Stephan Borrmann (stephan.borrmann@mpic.de)

Abstract. Aircraft borne in situ measurements of the chemical aerosol composition were conducted in the Asian Tropopause Aerosol layer (ATAL) over the Indian subcontinent in summer 2017 covering particle sizes below ~3 µm. We have implemented a recently developed aerosol mass spectrometer, which adopts the laser desorption technique as well as the thermal desorption method for quantitative bulk information (i.e. a modified Aerodyne AMS), aboard the high-altitude research aircraft M-55 *Geophysica*. The instrument was deployed in July and August 2017 during the StratoClim EU campaign (Stratospheric and upper tropospheric processes for better climate predictions) over Nepal, India, Bangladesh, and the Bay of Bengal, covering altitudes up to 20 km a.s.l.. For particles with diameters between 10 nm and ~3 µm, the vertical profiles of aerosol number densities from the eight research flights show significant enhancements in the altitude range of the ATAL. We observed enhancements in the mass concentrations of particulate nitrate, ammonium, and organics in a similar altitude range between approximately 13 km and 18 km (corresponding to 360 K and 410 K potential temperature). By means of the two aerosol mass spectrometry techniques, we show that the particles in the ATAL mainly consist of ammonium nitrate and organics. The single particle analysis from laser desorption and ionizaton mass spectrometry revealed that a significant particle fraction (up to 70 % of all analyzed particles by number) within the ATAL results from the conversion of inorganic and organic gas-phase precursors, rather than from the uplift of primary particles from below. This can be inferred from the fact that the majority of the particles encountered in the ATAL consisted solely of secondary substances, namely an internal mixture of nitrate, ammonium, sulfate, and organic matter. These particles are externally mixed with particles containing primary components as well. The single particle analyses suggest that the organic matter within the ATAL and in the lower stratosphere (even above 420 K) can partly be identified as organosulfates, in particular glycolic acid sulfate, which are known as components indicative for secondary organic aerosol formation. Also, the secondary particles are smaller in size compared to those containing primary components (mainly potassium, metals, and elemental carbon). The analysis of particulate organics with the thermal desorption method

shows that the degree of oxidation for particles observed in the ATAL is consistent with expectations about secondary organics that were subject to photochemical processing and ageing. We found that organic aerosol was less oxidized in lower regions of the ATAL (< 380 K) compared to higher altitudes (here 390 - 420 K). These results suggest that particles formed in the lower ATAL are uplifted by prevailing diabatic heating processes and thereby subject to extensive oxidative ageing. Thus, our observations are consistent with the concept of precursor gases being emitted from regional ground sources, subjected to rapid convective uplift, and followed by secondary particle formation and growth in the upper troposphere within the confinement of the Asian Monsoon Anticyclone (AMA). As a consequence, the chemical composition of these particles largely differs from the aerosol in the lower stratospheric background and the Junge layer.

1 Introduction

The Asian Tropopause Aerosol Layer (ATAL) develops every year inside the Asian Monsoon Anticyclone (AMA) during the summer monsoon period (i.e. between June and September) at altitudes between approximately 14 km and 18 km (Vernier et al., 2009, 2011, 2015, 2018; Thomason and Vernier, 2013; Yu et al., 2017; Brunamonti et al., 2018; Zhang et al., 2019). The geographical extent of the AMA can reach from the Eastern Mediterranean to Western China, and correspondingly the ATAL is spatially, temporally, and seasonally highly variable (Yuan et al., 2019; Hanumanthu et al., 2020). Due to internal dynamical variability, the location and the shape of the anticyclone change from day to day and oscillate between a state with one anticyclone and a different state with two separated anticyclones (so-called modes). The modes often are referred to as western (Iranian) and eastern (Tibetan) mode (e.g. Zhang et al., 2002; Vogel et al., 2015; Nützel et al., 2016) and they affect the spatial distribution of the ATAL as well. Widespread within the Asian monsoon region and its surroundings, there are numerous ground sources of natural emissions and anthropogenic pollution (e.g. Lawrence and Lelieveld, 2010). As the summer monsoon is accompanied by large-scale convection especially in the Himalayan region and the Tibetan plateau, strong upward transport carries trace gases, aerosols, and precursor gases of natural and anthropogenic origin from the boundary layer aloft to the altitudes of the AMA (approximately 12 to 20 km a.s.l.), and in parts beyond into the lower stratosphere (Randel et al., 2010; Pan et al., 2016; Vogel et al., 2019). Soluble substances and aerosol particles experience scavenging and chemical processing during the transport through convective mixed phase clouds. As a consequence, the chemical composition and abundance of materials which are amenable for the formation of the ATAL are altered and thus differ from the initial boundary layer conditions (Barth et al., 2001, 2007a, b; Tost et al., 2010; Bela et al., 2016; von Blohn et al., 2011, 2013; Jost et al., 2017; Lawrence and Lelieveld, 2010). These constituents reach the cloud detrainment zone between approximately 8 and 16 km a.s.l. and accumulate inside the AMA together with other pollution components which arrive here in parts unaffected by cloud processing. Above the convective outflow, the released emissions are rapidly oxidized by OH. The high abundance of NO_x especially from lightning enhances the recycling of OH radicals, leading to an increased oxidative capacity of the air in the anticyclone (Lelieveld et al., 2018). The described processes influence the chemical composition of the air circulating inside the AMA throughout its vertical profile (Randel and Park, 2006; Park et al., 2009; Randel and Jensen, 2013; Vogel et al., 2015;

Pan et al., 2016; Bucci et al., 2020) and provide precursor gases for secondary aerosol formation. Such precursor gases reach the upper troposphere (e.g. Höpfner et al., 2016, 2019; Fairlie et al., 2020), where homogeneous nucleation and subsequent particle growth processes form secondary particles in clear air as well as inside the outflows of convective cloud systems (Weigel et al., 2011, 2021a, b; Williamson et al., 2019). The exact details of the precursor gas mixture and the involved processes for inorganic homogeneous nucleation (including H_2SO_4, NH_3, HNO_3 among others), as well as secondary organic aerosol (SOA) formation still are unknown. However, mainly modeling studies show that the relevant aerosol components within the AMA are nitrates, ammonium, sulfates, as well as organics, mineral dust, black carbon (Fadnavis et al., 2013; Neely III et al., 2014; Yu et al., 2015; Gu et al., 2016; Lelieveld et al., 2018; Lau et al., 2018; Ma et al., 2019), some metals, and to a small extent meteoric dust as well (Schneider et al., 2021). In this context ammonium nitrate (AN) is of particular importance. As already pointed out by Metzger et al. (2002), the partitioning between the gas phase HNO_3 and NH_3 and its condensed phase NH_4NO_3 influences the atmospheric life time of these substances, since ammonium nitrate has a much longer residence time than its precursor gases. The authors concluded from their global model calculations (albeit with large uncertainties and without considering seasonal cycles) that an extended ammonium nitrate aerosol plume should exist in the upper troposphere at atmospheric pressure of 200 to 300 hPa (in a region characterized by efficient upward transport) from South Eastern Asia to Africa as result of ammonia ground emissions (mostly from agriculture) in India and Southern Asia. This was corroborated by satellite remote sensing as early as 1997 from the instruments CRISTA and MIPAS/Envisat (Höpfner et al., 2019), and by laboratory studies on the ammonia – nitric acid system (Wang et al., 2020). Additional experiments performed in the CLOUD chamber at CERN (Wang et al., 2022) under upper tropospheric conditions showed that new particle formation from the ternary H_2SO_4/HNO_3/NH_3 system occurs at nucleation rates which are orders of magnitude higher than for systems with any binary combination of these three gases. Further, Gu et al. (2016) concluded from GEOS-CHEM 3D model simulations that particulate nitrate in the PM2.5 range is a dominant component of the upper troposphere and lower stratosphere (UTLS) in the AMA region although it is not a major contributor to the boundary layer aerosol. According to their calculations, the nitrate fractions of the PM2.5 aerosol can be higher than 60% at the 100 hPa level while being below 5 – 25% near the surface. Balloon based in situ data reported by Vernier et al. (2018) provided first indications for the presence of nitrate aerosol in the ATAL. Finally, within the StratoClim project, remote sensing measurements from the aircraft borne (here the Russian M-55 *Geophysica* high-altitude research aircraft) near infrared spectrometer GLORIA by Höpfner et al. (2019), gave clear evidence for solid ammonium nitrate as a major component of the ATAL inside the 2017 AMA. In their study also first quantitative in situ measurements by means of our aerosol mass spectrometry were introduced, which unambiguously demonstrated the existence of a nitrate aerosol layer in the ATAL altitude range. Desert dust may also be a component of the regional UTLS aerosol and the ATAL. This was concluded from model simulations (Fadnavis et al., 2013; Lau et al., 2018; Yuan et al., 2019), although measurements and experimental quantification still are missing.

Aerosol size distribution measurements were concurrently performed on the M-55 *Geophysica* during StratoClim inside of the 2017 AMA by Mahnke et al. (2021), using optical particle counters (UHSAS-A and NIXE-CAS) for the size range of 65 nm to 3 $\mu\mathrm{m}$ in diameter. This range extends towards smaller particle sizes beyond the previous measurements by Yu et al. (2017), who adopted a balloon borne POPS optical particle counter with a lower size detection limit of 140 nm. As detailed in Mahnke

et al. (2021), additional data from the COPAS high-altitude condensation particle counter (Weigel et al., 2009, 2021a) allowed adding one broad size bin extending from 10 nm to 65 nm to the size distributions delivered by the UHSAS-A. By means of these composite size distributions from the three instruments (i.e. COPAS, UHSAS-A, and NIXE-CAS) covering 10 nm to ~3 µm aerosol back scattering ratios then could be derived and compared with the CALIOP satellite measurements of roughly the same time period as during StratoClim. The results from both methods agree well and exhibit an aerosol layer between 14 km and 18 km altitude inside the AMA (Mahnke et al., 2021). Thus, with respect to number density, the ATAL in 2017 consisted mainly of particles with diameters below 3 μm with a broad peak in the size distribution around 100 nm with the highest number densities near 40 000 cm^{-3} (Mahnke et al., 2021; Weigel et al., 2021a). Previous balloon borne observations also had indicated a maximum in the size distribution at diameters of around 100 nm (Yu et al., 2017; Vernier et al., 2018).

Diabatic vertical transport of air masses carries the aerosol particles of the ATAL aloft with slow (~1 – 1.5 K per day) vertical ascent rates in an anticyclonic large scale spiral movement (Vogel et al., 2019). These air masses cross the lapse rate tropopause which here in the tropics does not act as a transport barrier. Between approximately 380 K and 460 K of potential temperature isentropic mixing and "spiral stirring" with air masses from the neighboring regions occur. As a consequence of the arguments laid out for trace gases by Vogel et al. (2019), a probably small fraction of the contained aerosol can as well reach the tropical pipe and subsequently become globally distributed. Most likely, however, a larger part of the aerosol originating from the AMA is distributed together with other tropospheric constituents in the northern hemispheric extratropical lowermost stratosphere via quasi-isentropic transport (see e.g. Garny and Randel, 2016; Ploeger et al., 2017; Yu et al., 2017; Fadnavis et al., 2018). Since "eddy shedding" occurs a few times each summer (e.g. Popovic and Plumb, 2001; Vogel et al., 2014; Pan et al., 2016) parts of the accumulated aerosol particles and gases become amenable to distribution in the upper troposphere and for long range transport (see e.g. Lawrence and Lelieveld, 2010; Vogel et al., 2016; Fujiwara et al., 2021). As suggested by Yu et al. (2017), as much as 15 % of the northern hemispheric stratospheric aerosol surface area could originate in the AMA on an annual basis, albeit with considerable seasonal variability (Yuan et al., 2019). Whether or not the aerosol nucleated in the AMA is a source for the global stratospheric Junge layer is a still open and debated question. Some fraction of the freshly nucleated and aged particles inside the AMA are involved in ice cloud formation below the tropopause and in the tropical transition layer (Ueyama et al., 2018) as has been demonstrated by laboratory experiments for the case of ammonium nitrate aerosol (Wagner et al., 2020). Others may act as cloud nuclei further down in the tropical middle troposphere, which was suggested by Andreae et al. (2018) based on their measurements over the Amazon rain forest. For the higher altitudes the effects on the radiative budget and possibly heterogeneous chemistry (see e.g. von Hobe et al., 2011; Talukdar et al., 2012) are of concern. In general, aerosols in the UTLS are of relevance for the climate since the ice nucleation processes influence cirrus cloud properties (see e.g. Liu et al., 2009; Fadnavis et al., 2013) and thus their radiative effects. The extent of the regional radiative forcing at the top of the atmosphere in connection with the ATAL was estimated by Vernier et al. (2015) to be in the order of $-0.1\ \mathrm{W\,m^{-2}}$. Although considerable uncertainty still exists concerning the radiative forcing of the ATAL, from Ridley et al. (2014) it can be concluded that the radiative effects may be comparable to the global aerosol forcing (0.05 to 0.12 K) from moderate volcanic eruptions since 2000. Based on sensitivity studies using model simulations and satellite observations, Fadnavis et al. (2019) concluded that the regional upper tropospheric aerosol may aggravate the draughts over the Indian sub-continent during El Niño periods.

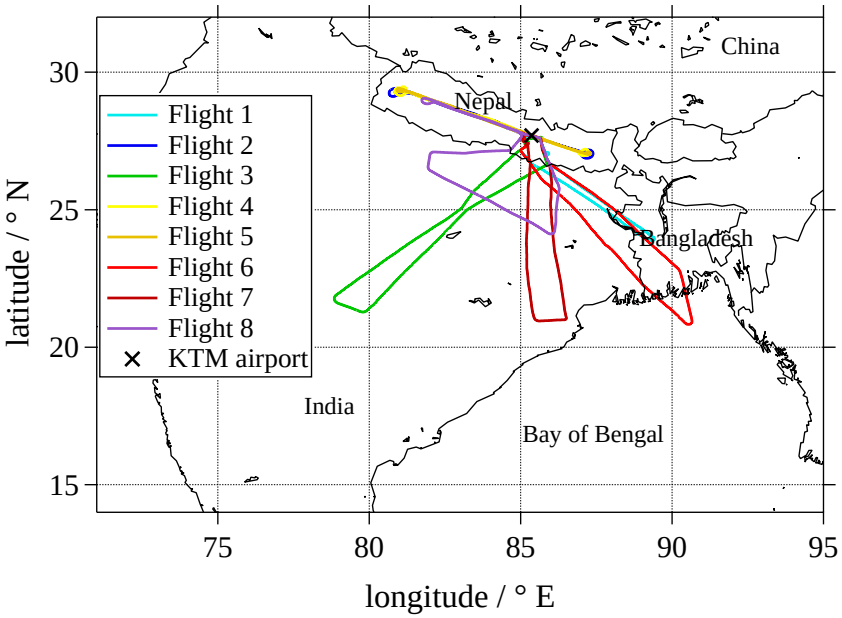

Figure 1. Paths of the eight research flights during the StratoClim field campaign 2017 over Nepal, India, Bangladesh, and the Bay of Bengal. The flight dates were Flight 1: 27 July, Flight 2: 29 July, Flight 3: 31 July, Flight 4: 2 August, Flight 5: 4 August, Flight 6: 6 August, Flight 7: 8 August, Flight 8: 10 August 2017.

In this study, we provide detailed observational data on the chemical aerosol composition of the ATAL and its surroundings from in situ measurements carried out on board the Russian M-55 *Geophysica* high-altitude research aircraft within the StratoClim project. While previous work has been focused on nitrate aerosol, we demonstrate here by means of quantitative and qualitative aerosol mass spectrometry that the ATAL not only contains ammonium nitrate particles but also a significant fraction of particulate organics, the properties of which also are subject of this study. Furthermore, the presented measurements include results for particulate sulfate within the AMA.

2 The StratoClim field campaign, measurement platform, and instrumentation

The measurements were taken in the framework of the StratoClim (see: http://www.stratoclim.org/, accessed on 27 Jan 2022) EU project with the goal to better understand the meteorological and chemical processes of the AMA. The base for the field campaign was the Tribhuvan International Airport (KTM) in Kathmandu, Nepal, where eight research flights were performed between 27 July and 10 August 2017. The adopted platform was the single-seated Russian high-altitude research aircraft M-55 *Geophysica*, which can carry a payload of up to 2000 kg to a nominal ceiling of 21 km. The eight research flights had a duration between 2 h 42 min and 4 h 28 min and the highest GPS altitude reached during StratoClim was ~~20.0 km~~20.5 km. Fig. 1 shows the flight paths for the StratoClim aircraft campaign 2017 over Nepal, India, Bangladesh, and the Bay of Bengal.

In situ aerosol mass spectrometry: For in situ measurements of the aerosol chemical composition, the newly developed ERICA instrument (ERC Instrument for the Chemical composition of Aerosols) was implemented on the M-55 *Geophysica* (Hünig et al., 2022; Dragoneas et al., 2022). The two commonly adopted methods for in situ real-time mass spectrometric analysis of aerosol particles are (1) laser desorption ionization (LDI) of particles followed by time-of-flight mass spectrometry (Suess and Prather, 1999), and (2) thermal desorption with subsequent electron impact ionization (TDI) as implemented in the Aerodyne AMS (Drewnick et al., 2005; Canagaratna et al., 2007). The ERICA combines these two techniques in a single, fully automatically operating apparatus. The instrument has been described in detail by Hünig et al. (2022) and Dragoneas et al. (2022) and is only briefly reviewed here:

Ambient sample air is supplied to the ERICA by a specially designed shrouded inlet (Dragoneas et al., 2022), which consists of a two-staged diffusor that reduces the required sampling line velocity for isokinetic sampling by a total factor of 39. The principal design is based on the aerosol inlet used in the IAGOS-CARIBIC project (Brenninkmeijer et al., 2007) and for the ERICA the inlet design and its performance has been simulated by computational flow dynamics. Before entering the mass spectrometer, the sample air passes through a pressure-regulating critical orifice (Molleker et al., 2020) which ensures the reliable performance of the aerodynamic lens (Peck et al., 2016) at the entrance of the ERICA. The critical orifice maintains a constant mass flow or normal volumetric flow (referenced to normal temperature and pressure NTP: 20 °C and 1013.25 hPa) of 1.45 $\mathrm{cm^3\,s^{-1}}$ into the instrument. The aerodynamic lens is designed to be operated at a pressure of 4.53 hPa, provided by a critical orifice with a diameter of ~100 µm at ground level, which increases to ~400 µm at lower stratospheric ambient pressures of 60 hPa.

The ERICA-LAMS (ERICA laser ablation mass spectrometer) unit implements the LDI technique. Two continuous wave lasers detect and classify the individual particles by size and are used to trigger a pulsed UV desorption/ionization laser (Hünig et al., 2022), similar to, e.g. the ALABAMA (Brands et al., 2011) or the PALMS (Murphy, 2007) instruments. The vacuum aerodynamic diameter of the particles (d_{va}) is derived from the particle velocity by applying a calibration with particles of known diameter, density, and shape (here, monodisperse polystyrene latex particles in a diameter range between 80 nm and 5.1 µm (Hünig et al., 2022)). The ions generated by the UV laser pulse (~4 mJ at a wavelength of 266 nm) are extracted by switched electrical fields to generate positive and negative ion mass spectra for each desorbed aerosol particle. Due to a relatively long idle time of >120 ms of the desorption laser, most particles continue flying unaffected downstream in the vacuum chamber towards the ERICA-AMS unit. They hit a tungsten vaporizer, where the non-refractory components are vaporized at around 600 °C. The vapour is ionized by means of the electron impact method and a CTOF-MS (compact time-of-flight mass spectrometer) is used to generate uni-polar positive mass spectra of small particle ensembles.

The particle size range detectable by the ERICA-AMS is given by the transmission efficiency of the aerodynamic lens (vacuum aerodynamic diameter of the particles between 110 nm and 3.5 µm, Xu et al. (2017)). Although Hünig et al. (2022) indicates an even lower cutoff of less than 90 nm, the smallest particles will not significantly contribute to the mass concentrations measured by the ERICA-AMS during StratoClim. The lower cutoff diameter of the LDI unit is limited by the optical particle detection efficiency to 180 nm. The short passage through the inlet and tubing does not significantly alter the detectable size

range and the losses have been estimated to be below 20 % for particles up to 3 µm even at low ambient pressures of 65 hPa (Dragoneas et al., 2022).

The data of the ERICA-AMS are processed with TofWare 2.5.7 (Tofwerk) as detailed in the Supplement Sect. S1.1 and S1.2. The detection limits of the mass concentrations are calculated from the background measurement with closed shutter as in Drewnick et al. (2009), however in this publication we analyze the background noise using a Savitzky-Golay (SG) filter (Savitzky and Golay, 1964). The method is further described in Supplement Sect. S1.3 and is similar to those adopted by Reitz (2011) and Schulz et al. (2018). During the StratoClim aircraft campaign 2017, we found an average detection limit of 0.12 µg m^{-3}(NTP) for nitrate, 0.13 µg m^{-3}(NTP) for sulfate, 0.50 µg m^{-3}(NTP) for organics, and 0.73 µg m^{-3}(NTP) for ammonium, each representative for a sampling period of 10 s, i.e. one measurement cycle consisting of aerosol and background measurement. For longer averaging times t (e.g. the total residence time in a certain altitude or θ bin), the detection limit scales with $1/\sqrt{t}$. The detection limits are comparable to values determined with the common filter method during ground measurements as shown by Hünig et al. (2022).

Single-particle mass spectra were obtained by the ERICA-LAMS. Considering only spectra sampled outside of clouds, a total of 109 453 spectra were analyzed from the StratoClim data set; 99 % of the spectra include size information and 92 % of the spectra have dual polarity. We used the software package CRISP (Concise Retrieval of Information from Single Particles; Klimach, 2012) to perform m/z (ion mass to charge ratio) calibration, peak area integration, and particle classification. Particles were classified by a combination of fuzzy-c means clustering (Hinz et al., 1999; Roth et al., 2016; Schneider et al., 2021) and the marker ion method (Köllner et al., 2017, 2021). For this study, we classified particles in two main categories: particles containing solely components typical for secondary formation like nitrate, sulphate, and organics (Secondary Type) and particles containing a mixture of secondary as well as primary components like soot, metals, salt, and organics from biomass-burning (Primary or Mixed Type). Details on the classification methods of the particles can be found in the Supplement Sect. S2.1. As a next step, the fraction and scaled number concentrations of the particle types are determined. For the calculation of particle fractions, we summed up total analyzed particles (i.e. detected, desorbed, and ionized) and particles from a specific type in certain bins of variables (here, altitude, potential temperature, and d_{va}). For each bin, we divided the number of particles of a specific type by the number of all analyzed particles, providing the particle number fraction (PF). Further, by multiplying with the measured particle number concentration at the first detection stage (N_0) of the ERICA, we acquire the scaled number concentration of a specific particle type ($PF \cdot N_0$). This scaling method assumes that the hit rate of the ERICA-LAMS is independent on particle characteristics, such as size, composition, and shape. However, earlier studies show that this is not the case (Thomson et al., 1997; Kane et al., 2001; Moffet and Prather, 2009; Brands et al., 2011). As a result, we only discuss the variation in the scaled number concentrations as a function of other parameters (here: altitude and potential temperature), rather than discussing the absolute values of number concentrations.

Aerosol size distribution and cloud particle measurements: A modified UHSAS-A optical particle counter covering a nominal particle diameter from 65 nm to 1 µm was deployed on the aircraft as an underwing probe for aerosol size distribution measurements. As described in more detail by Mahnke et al. (2021), for the operation of the UHSAS-A at atmospheric

pressures below 130 hPa several modifications, e.g. of the flow system, had to be implemented to ensure reliable performance under the ambient conditions encountered during StratoClim.

A CDP optical wing ~~sonde~~ probe (Cloud Droplet Probe from Droplet Measurement Technologies, Longmont, CO, USA) with a diameter range from 2.5 µm to 46 µm was used to detect the presence of cloud and ice particles. In this study, the CDP has been used to identify cloud passages (i.e. periods with ice water contents above 0.1 $\mathrm{mg\,m^{-3}}$, averaged over 11 seconds) and exclude single particle spectra and ERICA-AMS data during the passages from our analysis to avoid potential artefacts from the inlet system like droplet impact or ice shattering.

The number concentrations of aerosols with sizes down to nucleation mode were determined with the four-channel flow-through condensation particle counter COPAS (COndensation PArticle counting System). COPAS is operated with a chlorofluorocarbon (FC-43) as the working fluid, its particle detection and data storage occur with a temporal resolution of maximum 1 Hz. Three COPAS channels operate with 50 % detection particle diameters $d_{p,50}$ of 6 nm, 10 nm and 15 nm, respectively. The fourth COPAS channel (with $d_{p,50}$ = 10 nm) detects particles after their exposure to temperatures of 270 °C by means of a heated sample flow line. In this way, particle concentrations of non-volatile (nv) or refractory particles (e.g. soot, mineral dust, metallic aerosol material, etc.) are determined. The counting performance of COPAS under variable pressure conditions is described by Weigel et al. (2009), and its capabilities have been demonstrated in several deployments of COPAS associated with the M-55 *Geophysica* (see Borrmann et al., 2010; Weigel et al., 2011, 2021a, b, and references therein)

Other instruments and methods: Ambient temperature T and pressure p as well as coordinates (GPS altitude, latitude, longitude), and aircraft specific data like roll and pitch angle, were supplied by the UCSE unit (Unit for Connection with the Scientific Equipment; Sokolov and Lepuchov, 1998) from the aircraft's avionic system. The accuracies for the 1 Hz-resolved UCSE data are ± 1 hPa and ± 2 K for the ambient pressures and temperatures, respectively. The potential temperature θ has been calculated from the aircraft data acoording to $\theta = T \cdot (\frac{1000\,\mathrm{hPa}}{p})^{\frac{R_L}{c_p}}$ with the specific gas constant $R_L = 287.058\,\mathrm{J\,kg^{-1}\,K^{-1}}$ and specific heat capacity $c_p = 1005\,\mathrm{J\,kg^{-1}\,K^{-1}}$.

For measurements of NO with SIOUX, a chemiluminescence technique is adopted. Here, a cooled photomultiplier detects the light emission from the reaction of NO with ozone (O_3). O_3 is produced in the instrument by a dielectric barrier discharge. The detector is identical to the one used for measurements from an in-service aircraft during more than 460 flights since 2005 (CARIBIC Project) and is described in detail by Stratmann et al. (2016). The precision and accuracy of the SIOUX NO measurements are 7 % and 10 %, respectively. The NO detection limit is 3 pptv.

3 Results and discussion

3.1 Chemical composition of the ATAL aerosol particles as measured by the ERICA-AMS

The ERICA-AMS provides mass concentrations of particulate organics, nitrate, sulfate, and ammonium. Figure 2 shows the median mass concentrations as function of altitude and potential temperature (θ) together with the $25th$ and $75th$ percentiles.

The profiles of the eight individual research flights are provided in the Supplement Sect. S3.1. Based on the distribution of our in situ mass concentration measurements, several atmospheric layers can be identified:

1. The boundary layer (BL) with increased mass concentrations below 320 K,
2. The free troposphere (FT) between 320 K and 350 K with low values for the mass concentrations ($< 0.5\,\mu g\,m^{-3}$(NTP))
3. The ATAL between 355 K and 420 K. This is comparable to the altitude range of the ATAL given in Vernier et al. (2011) of 13 to 18 km (corresponding to ~360 - 410 K during StratoClim) detected by the satellite based Lidar instrument CALIOP (Cloud-Aerosol Lidar with Orthogonal Polarization).
4. Above 420 K, mostly sulfate aerosol is detected, which is a typical characteristic of the lower stratosphere (LS).

According to European Centre of Medium-Range Weather Forecasts (ECMWF), ERA-Interim reanalysis data for the time period of the research flights, the lapse rate tropopause was between 369 K and 396 K of potential temperature with a mean level of 380 K. Thus, the aerosol layer visible in the mass concentration data extends well into the LS. The top of the AMA system confinement in 2017 was found at roughly 420 K by means of in situ trace gas measurements (von Hobe et al., 2021) on the M-55 *Geophysica*. This level of potential temperature coincides with a significant decrease in the particle number concentrations towards stratospheric values as reported by the COPAS condensation particle counter for particles with diameters between 10 nm and 1 µm (Mahnke et al., 2021; Weigel et al., 2021a). Including deep convection the region of convective outflows extends from about 12 km to 17 km – approximately corresponding to θ levels between 360 to 385 K – with a maximum intensity around 14 km. Based on back-trajectory analyses and satellite observations, Bucci et al. (2020) concluded for the period of the StratoClim aircraft campaign 2017 that the age of air up to 15 km is rarely more than 5 days and that these young air masses dominate the air composition here. Bucci et al. (2020) also identified a transition layer between 15 km and 17 km with ages of air masses between one and two weeks. In this transition region convection still is the major contributor of air masses. Above 17 km, the mean age of the sampled air is ~20 days with the convective contribution decreasing to zero around 20 km. Thus, the ATAL layer discernible in Fig. 2 is situated in an altitude region with air of several weeks of age, which still is strongly influenced by deep convection. In this meteorological situation of the AMA in 2017, organic and inorganic precursors for secondary aerosol formation, as well as primary particles originating from below easily reach the altitudes of the ATAL. ~~Consequently, the ATAL chemical composition is largely determined by the relative contributions of new particle formation and secondary particle growth at altitude compared to the upward transport of already nucleated secondary or of primary particles from below.~~

The vertical profiles in Fig. 2 show clear enhancements of aerosol mass concentrations in the UTLS, especially for particulate organics, nitrate, and ammonium. In the ATAL altitude range, the vertical number density profiles of submicrometer sized particles, as concurrently measured by the COPAS and the UHSAS-A, also exhibit significantly elevated values with respect to the middle troposphere and the lower stratosphere (Mahnke et al., 2021; Weigel et al., 2021a). This is evident from Fig. 3, which is a comprehended representation of the data from their studies, and which shows the results of particle number concentration larger than 10 nm and larger than 65 nm as a function of altitude and potential temperature. In these publications

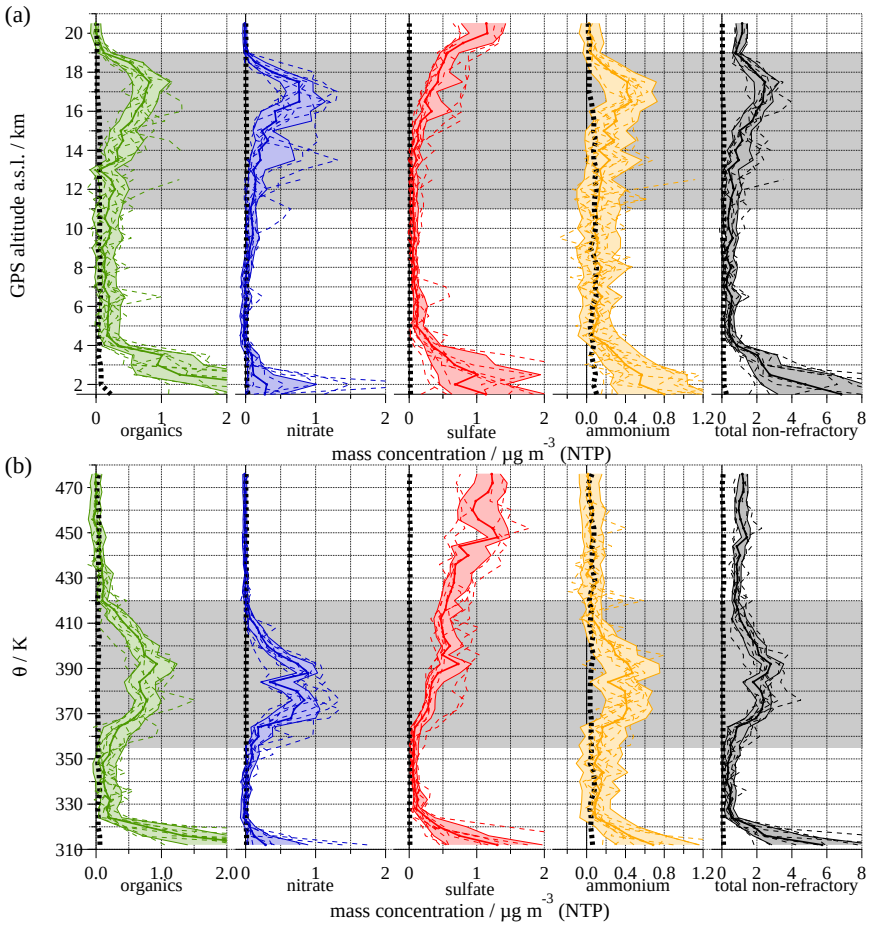

Figure 2. ERICA-AMS mass concentrations of particulate organics (green), nitrate (blue), sulfate (red), and ammonium (orange) as a function of (a) GPS altitude and (b) potential temperature θ. The thick line and the shaded area represent the median and $25th/75th$ percentiles in the corresponding altitude or θ bin of the entire StratoClim aircraft campaign 2017. The dashed lines represent the median of each individual research flight. The right panel displays the sum of all species measured by the ERICA-AMS (black). The shaded background indicates the approximate altitude range of the ATAL. For each altitude bin the detection limit is displayed as a dotted line close to the ordinate. Concentrations in the boundary layer can exceed the displayed range.

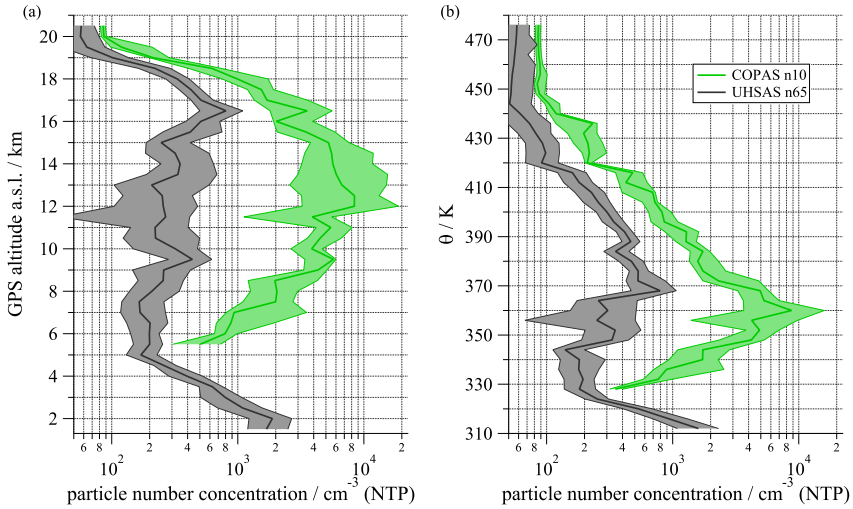

Figure 3. Vertical profile of the median submicron aerosol particle number concentrations as measured by the COPAS and the UHSAS-A (n10, n65: particles with diameters larger than 10 nm and 65 nm, respectively) as a function of (a) GPS altitude and (b) potential temperature θ.

and in Weigel et al. (2021b), it was demonstrated that new particle formation and subsequent particle growth by condensation and coagulation can be frequently observed in the lower ATAL region below the tropopause (between 355 and 370 K). Note however, that COPAS data for particles between 6 and 10 nm in diameter – indicative of such transient new particle formation events – are not included in Fig. 3. Thus, the ATAL in the 2017 AMA could be identified by all of our in situ aerosol particle instruments aboard the M-55 *Geophysica* as enhancements in the respective vertical profiles. Remarkably, the vertical profile of sulfate (mostly as ammonium sulfate below 400 K potential temperature, see Fig. 6) does not show a peak in the ATAL region. It steadily increases towards the stratosphere becoming the dominant aerosol constituent above 420 K. This is interesting, because several studies in the literature (e.g. Neely III et al., 2014; Yu et al., 2017; Vernier et al., 2015) hypothesized sulphur dioxide to be a main precursor for the ATAL layer formation, which is not unreasonable considering the high level of regional anthropogenic SO_2 emissions. However, for the particles in the ATAL of the AMA 2017, nitrate and organics are the major constituents. The vertical transport above 360 K, across the tropopause and up to ~460 K is driven by diabatic heating in an upward spiralling anticyclonic motion (Vogel et al., 2019). The observed increase in sulfate mass concentration is inside this upward spiralling range with growing ~~influence~~presence of the stratospheric background aerosol at the higher altitudes, because lower stratospheric air increasingly mixes with the upward transported AMA air masses (Vogel et al., 2019).

In terms of absolute values, the ERICA-AMS measurements show increased total mass concentrations in the altitude range of the ATAL (grey shaded area in Fig. 2) with a maximum of more than 2 $\mu g\,m^{-3}$(NTP). We found detectable concentrations of particulate nitrate up to 19 km a.s.l. or 420 K in potential temperature by means of the ERICA-AMS, whereas particulate organics even reach 19.5 km or 430 K. Thus, regarding the main particle components, we can determine the upper boundary of the ATAL to be higher than 18 km, which is the upper boundary as detected by satellite observations (Vernier et al., 2011).

Figure S1 in the Supplement demonstrates the average potential temperature and vertical spread-out of the organics profile to be larger than for the nitrate layer. At the lower boundary of the ATAL, the nitrate signal shows an increase with altitude at 8 km, when averaging over the whole campaign. However, during some flights no nitrate signal was detected below 13.5 km. Overall, the concentrations and vertical distributions varied strongly from day to day (dashed lines in Fig. 2 and Fig. S2-S9 in the Supplement). While this can in general be explained by different flight paths, Hanumanthu et al. (2020) found similar day-to-day variations for the total mass concentration detected over the foothills near Nainital, India during a balloon campaign in August 2016. Nitrate contributes about 30 % to the non-refractory mass of the ATAL. This is more than common fractions of nitrate obtained during boundary layer measurements in Asia (Zhou et al., 2020) or other parts of the world (Jimenez et al., 2009), even though the occurrence of nitrate aerosol is generally associated with agricultural emissions in the boundary layer (e.g. Hock et al., 2008). Together with the sufficiently available ammonium (see Section 3.2), it can be assumed that the nitrate found in the ATAL is predominantly existent in the form of ammonium nitrate (AN). A first quantification of particulate AN concentrations during StratoClim was obtained by Höpfner et al. (2019), who used the limb sounding instrument GLORIA as well as data from the ERICA-AMS. The concentrations measured by the two instruments show a good agreement between the instruments, which operate on very different physical principles. Concerning the particle phase, they concluded that the AN particles are solid based on their GLORIA measurements, dedicated AIDA chamber laboratory studies, and single particle aerosol mass spectra delivered by the ERICA-LAMS. The high abundance of AN is a distinguishing property of the ATAL aerosol. The median concentration of particulate nitrate shows a maximum of about 0.8 $\mu g\,m^{-3}(NTP)$ around 17 km or 370-390 K during the StratoClim aircraft campaign 2017. Höpfner et al. (2019) emphasized the importance of AN, but not only nitrate is enriched here. Organics – which are not detected by the GLORIA instrument – contribute similar amounts to the particulate mass concentration and may play a similar role for the ATAL. One could even imagine a very faint "organic ATAL" without AN, which could have formed in periods with low emissions of ammonia from agricultural activities.

As the AMA supports an accumulation of precursor gases and aerosol particles, it is worthwhile investigating the spatial distribution of the measured aerosol chemical properties. A suitable parameter for this is the equivalent latitude (EQL) as introduced by Ploeger et al. (2015), which defines the distance from the centre of the AMA based on gradients of potential vorticity. The value of 90° for EQL designates the centre of the AMA with decreasing values indicating growing distance. For Fig. 4, we binned averages of the measured organic and nitrate mass concentrations with respect to EQL (2° per bin) and potential temperature θ (5 K per bin). Figure 4b~~)~~ shows, that the highest concentrations of nitrate appear in the central region of the monsoon anticyclone. The mass concentration of particulate organics shows a broader distribution in vertical as well as horizontal extension (Fig. 4a~~)~~). However, these results represent only a brief period of the AMA and the underlying dynamics of the anticyclone may well lead to very different distributions in the course of time. ~~Nevertheless, the data show that the ATAL for the time of StratoClim was not only confined in the vertical direction but also indicates a decrease towards the edge of the AMA in the horizontal distribution.~~ A clear horizontal confinement of the ATAL can not be discerned from the graph. This might have been different, if the data base had been larger.

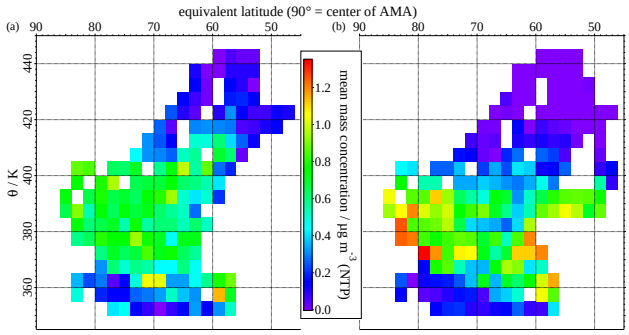

Figure 4. Curtain plot of (a) organic and (b) nitrate mass concentration as a function of θ and equivalent latitude (AMA-centred). The values for organics are based on the data from the Flights 1, and 4 through 8.

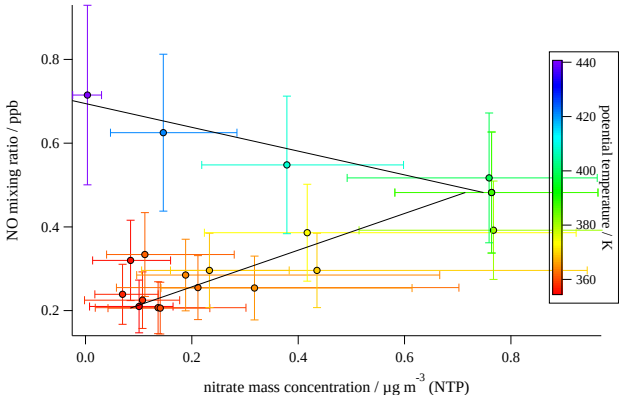

Figure 5. Nitrate mass concentration measured by the ERICA-AMS plotted against NO mixing ratio of SIOUX. The regression lines are shown to indicate the trends and are based on values for altitudes 10-17 km and 17-19 km, respectively. The horizontal bars reflect the 25th to 75th percentile range for nitrate and the vertical bars present an uncertainty of 30 % for NO.

3.2 Acidity of the ATAL aerosol

In the Asian monsoon region, NO_x is likely to be abundant due to anthropogenic emissions as well as from lightning (Tost, 2017; Fairlie et al., 2020; Metzger et al., 2002; Lelieveld et al., 2018) ~~(Stratmann et al., 2021)~~, reacting with water to form HNO_3. In fact, in situ measurements of NO as measured by SIOUX during Stratoclim showed enhanced concentrations in the ATAL with volume mixing ratios above 0.5 ppbv at altitudes between 16 and 18 km ~~(Stratmann et al., 2021)~~. This is demonstrated in Fig. 5 where the particulate nitrate mass concentration is plotted against the gas phase NO mixing ratio, colour coded with potential temperature θ. Between ~360 K and 400 K, NO is increasing with altitude and with particulate nitrate mass (lower regression line in Fig. 5) since this altitude band roughly corresponds to the outflow region of the convective clouds with lightning activity. Above ~400 K and in the lower stratosphere, NO increases further as result of the photolysis of

nitrous oxide (N_2O) while the particulate nitrate mass declines (upper regression line in Fig. 5). The formation of particulate nitrate usually requires nitric acid to find a reaction partner to form a less volatile substance. The capability of the gas phase constituents ammonia and nitric acid for homogeneous nucleation of new particles consisting of ammonium nitrate (followed by fast post-nucleation growth) has been demonstrated and studied in dedicated laboratory experiments by Wang et al. (2020). Even though ammonia is soluble in water and can thus be scavenged by precipitation during convective uplift, a low retention coefficient in the ice phase (Hoog et al., 2007; Jost et al., 2017; Ge et al., 2018) can play a role for ammonia reaching altitudes of cumulonimbus outflows in significant quantities especially during the Asian monsoon with prevalent deep convective clouds. Höpfner et al. (2016, 2019) demonstrated the occurrence of ammonia from agricultural sources above the convective outflow and also the influence of ammonia to the formation of ammonium nitrate in the ATAL.

The stoichiometric ratio of nitrate and sulfate on one hand, and ammonium, which can neutralize these species, on the other hand provides an indication on the acidity of the aerosol (Zhang et al., 2007). The mass concentration of ammonium can directly be measured with the ERICA-AMS, while the concentration of nitrate ($[NO_3]$) and sulfate ($[SO_4]$) determine the concentration of ammonium required for neutralization $[NH_{4,req}]$ according to:

$$[NH_{4,req}] = \frac{36}{96} \cdot [SO_4] + \frac{18}{62} \cdot [NO_3] \quad (1)$$

Figure 6 shows the vertical profile of $[NH_4]$ and $[NH_{4,req}]$ against altitude and potential temperature. The aerosol particles can be considered as fully neutralized, if the measured ammonium concentrations are in agreement with $[NH_{4,req}]$ in the corresponding bin. However, the neutralization balance of organics could not be included in the analysis due to the lack of the required data. Particles up to altitudes of 18 km or a potential temperature of 400 K contain approximately sufficient ammonium to neutralize the nitrate and sulfate content. Up to 19 km or 410 K, ammonium is still above the detection limit, but insufficient for the neutralization of the observed nitrate and sulfate. For higher levels, no particulate ammonium was detectable, in agreement with the observations of sulfuric acid in the stratosphere (e.g. Murphy et al., 2014). In essence, the vertical transport of ammonia and/or ammonium reaches altitudes up to 19 km influencing the aerosol acidity.

3.3 Secondary organic and inorganic particles within the ATAL

In this section, we discuss the role of secondary particle formation for the chemical composition and physical properties of the ATAL. The ERICA-AMS is not suited to detect refractory material like dust, metals and salt, which usually are indicative for the presence of primary aerosol particles. Non-refractory nitrate and sulfate as detected by the ERICA-AMS mostly represent secondary aerosol, however it can not be differentiated between pure secondary particles or coatings of nitrate and sulfate on pre-existing primary particles. The complementary single particle analysis by the LDI technique (here the ERICA-LAMS) allows us to study the internal mixing state of individual particles present in the ATAL. The mean bipolar single particle mass spectra of the Secondary and the Primary or Mixed ~~particle~~ Types (definitions see Sect. 2) are provided in Figs. 7 and 8. To note, we averaged over the entire single particle data set during StratoClim 2017, excluding data inside clouds. The Primary/Mixed Type is characterized by the detection of primary species like potassium and elemental carbon in the BL and ATAL region, along with sodium, other minerals, and anthropogenic metals in the BL (Figs. 8b and 8c). In the stratosphere

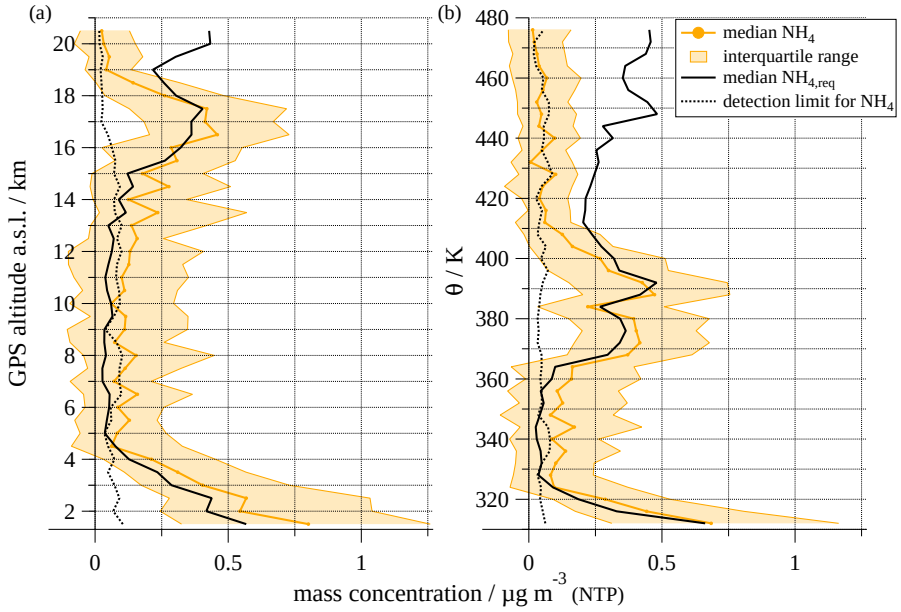

Figure 6. Vertical profile of the mass concentration of particulate ammonium (orange) with median and interquartile ranges measured by the ERICA-AMS as well as the median calculated ammonium required for full neutralization of the inorganic components ($NH_{4,req}$, black line) as a function of (a) GPS altitude and (b) potential temperature θ. The shaded areas delineate the $25th$ and $75th$ percentiles, and the detection limit of ammonium is shown as a dotted line.

above 420 K, primary particles are mainly composed of meteoric material (Fig. 8a; see also Schneider et al., 2021). However, as evident from the negative ion spectra, these particles are typically coated with secondary substances, such as sulfate and nitrate (Fig. 8). The identification of such mixing states requires the ability to record both ion polarities for each individual analyzed aerosol particle. Particles identified as Secondary Type are characterized by an internal mixture of solely secondary species, namely nitrate (m/z +30 (NO^+) and -46 (NO_2^-)), ammonium (m/z +18 (NH_4^+)), sulfate (m/z -97/99 (HSO_4^-)), and organic matter (m/z +27 ($C_2H_3^+$) and +29 ($C_2H_5^+$), likely from alkyl fragments (Silva and Prather, 2000); see Fig. 7). Hence, the so defined Secondary ~~particle~~ Type is not internally mixed with primary particle components. Further, we separated the Secondary ~~particle~~ Type into Type 1 and Type 2. Type 1 is characterized by a dominant NO^+ signal, whereas Type 2 shows organic peaks in the same order of magnitude as NO^+ (Fig. 7). Figure 9 presents the occurrence of Secondary ~~particle~~ Types 1 and 2 as a function of altitude and potential temperature. This figure shows the cumulative particle fraction (PF, left panels) and the scaled number concentration ($PF \cdot N_0$, right panels) of the two particle types ~~(definition see Sect. 2)~~. The size-resolved particle fraction of these particle types is given in Fig. 10. Note that in Fig. 10 the Primary/Mixed ~~particle~~ Type is restricted to particles found in the ATAL, since boundary layer aerosol and meteoric dust are not in focus of this study.

We found that the Secondary ~~particle~~ Type 1 is predominantly abundant within the ATAL, with a maximum particle fraction of 70 % by number (Fig. 9). In contrast, in the BL and FT, the abundance of ~~particle~~ Type 1 is low, while the ~~particle~~ Type

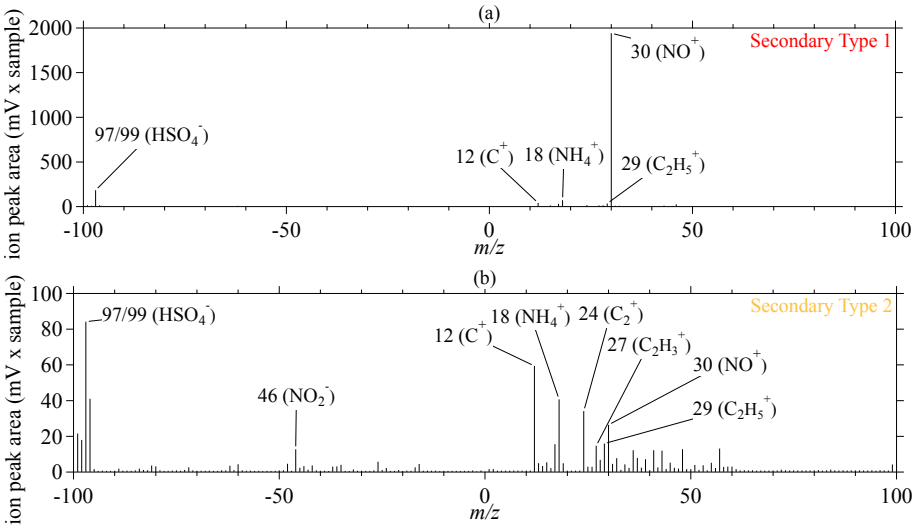

Figure 7. Bipolar mean spectra of the ERICA-LAMS particle types: (a) Secondary Type 1 (averaged over 33420 particles), (b) Secondary Type 2 (averaged over 6219 particles).

2 shows maximum fraction and number concentration. With increasing altitude within the ATAL, the abundance of Type 1 is increasing and reaches maximum values between 380 and 400 K (between 17 and 18 km). Above 400 K potential temperature, the abundance of ~~particle~~ Type 1 is again decreasing with θ and in the lower stratosphere (above 440 K) this particle type is not ~~evident~~found. Thus, the Secondary ~~particle~~ Type 1 (with the dominant NO^+ ion peak in the cation spectrum) is the dominant particle type in the ATAL region, consistent with the high mass fraction of AN measured by the ERICA-AMS. Nevertheless, particles containing primary components are present within the ATAL (Figs. 8b and 9). However, these particles also contain secondary material similar to the purely Secondary Type 1 (Fig. 8b) and contribute only a minor fraction to the number of analyzed particles between 370 and 400 K (Fig. 9b). Together, the external mixing of the Secondary ~~particle~~ Type 1 and the Primary/Mixed Type suggests that the dominant fraction of particles within the ATAL is formed via secondary processes, hence, independent of pre-existing transported primary particles. Consistent with this result, the size distribution of the Secondary Type 1 exhibits smaller diameters compared to the distribution of primary particles in the ATAL (Fig. 10).

The single particle analysis of Secondary ~~particle~~ Type 1 shows the presence of particulate organics in the ATAL (Fig. 7a). By using the ERICA-AMS measurements, we further investigate whether these organics result from primary emissions or secondary formation. For each data point, the fraction of the organic signal at m/z +44 to the total organic signal (f_{44}) is plotted against the fraction of organic m/z +43 to total organic signal (f_{43}) in Fig. 11. The relationship between f_{44} and f_{43} is a proxy for the degree of oxidation of organic aerosol particles (see Supplement Sect. S1.6 and Ng et al. (2010)). We averaged the data over 90 s and only displayed values where the total organic signal as well as the organic signals at m/z +43 and +44 are above the detection limit, since fractions of numbers below the limit of detection are very noise sensitive and contain no information. Figure 11 additionally shows median and interquartile ranges of f_{44} and f_{43} for different altitude regimes (BL, lower ATAL,

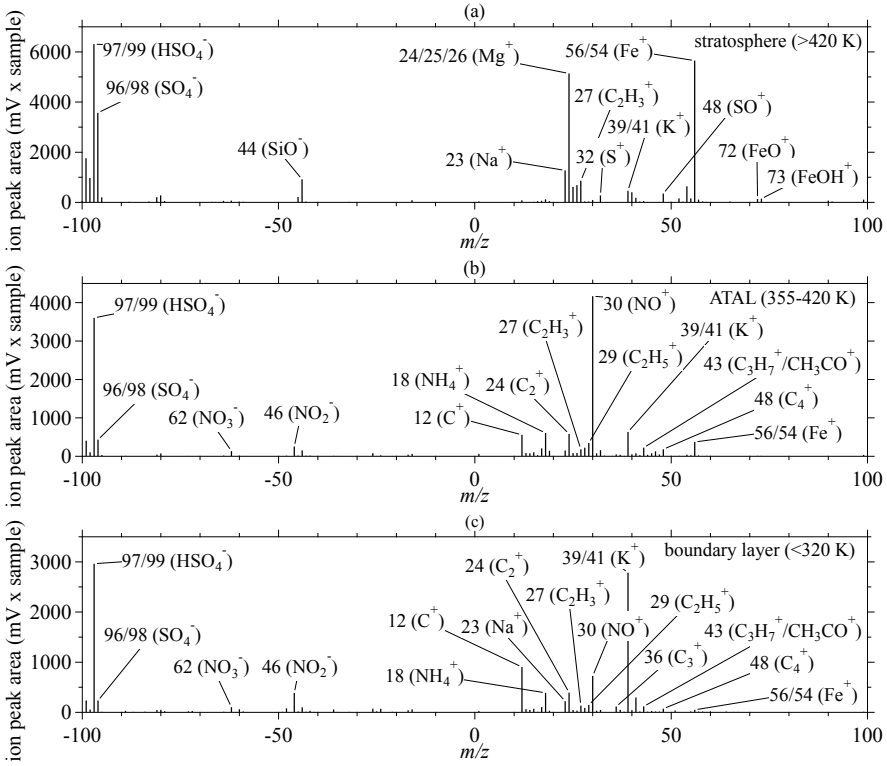

Figure 8. Bipolar mean spectra of the ERICA-LAMS particles containing primary components (Primary/Mixed Type): (a) in the stratosphere (averaged over 22493 particles), (b) in the ATAL (averaged over 16061 particles), and (c) in the boundary layer (averaged over 12044 particles).

middle ATAL, upper ATAL). The organic aerosol within the ATAL shows a large variety in values of f_{44} and f_{43}, which indicates the presence of aerosol particles with a wide range of ageing-states and/or from different sources (Ng et al., 2010, 2011). However, our observations of high f_{44} (>0.05) and low f_{43} values are consistent with expectations about secondary organics that have experienced oxidative ageing, as demonstrated by Ng et al. (2011). Together with the single particle measurements, we thus have several indications suggesting that the ATAL composition is to a large part controlled by secondary organic and inorganic aerosol formation. Our findings complement concurrent in situ observations of particle microphysical properties by Mahnke et al. (2021) and Weigel et al. (2021b), demonstrating that new particle formation and subsequent particle growth by condensation and coagulation takes place in the lower ATAL region below the tropopause (see Fig. 3).

~~The chemical nature of the ATAL has been subject of controversial discussions in the past decade. Modelling and observational (including satellites) studies provided evidence that main constituents are sulfates, organics, nitrates, and ammonium (Fadnavis et al., 2013; while others discussed the importance of mineral dust and black carbon aerosol (Fadnavis et al., 2013; Fadnavis et al., 2018; Fadnavis et al., Our in situ observations of particle composition, including primary and secondary components, show for the first time that the~~

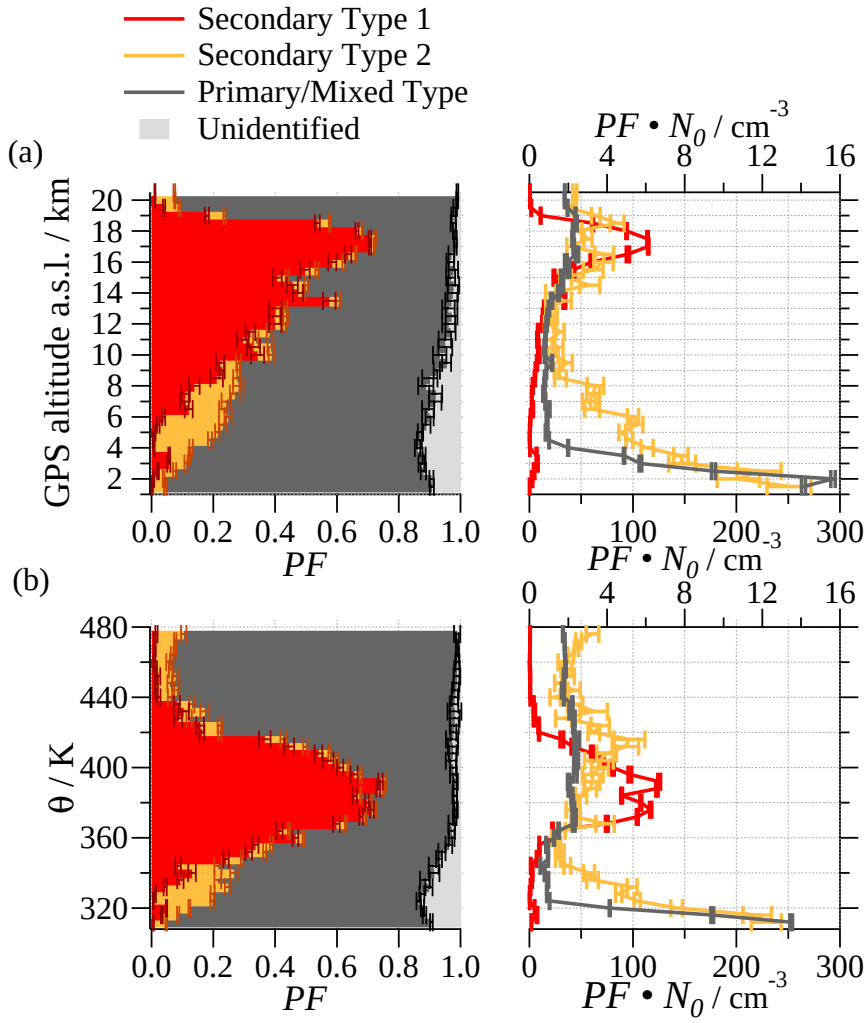

Figure 9. Vertically resolved fraction and number concentration of the identified particle types measured by the ERICA-LAMS as a function of (a) GPS altitude and (b) potential temperature θ. The identified particle types are: Secondary Type 1 (red), Secondary Type 2 (orange), and Primary or Mixed Type (dark grey). The unidentified particles are given in light grey in the left panels (see Supplement Sect. S2.1). The left panels represent the cumulative particle fractions (PF) of the particle types. The right panels represent the scaled ERICA-LAMS number concentrations ($PF \cdot N_0$) of the particle types. In the right panels, the top axis refers to the Secondary ~~particle~~ Type 2 and the bottom axis refers to the Secondary ~~particle~~ Type 1 and the Primary or Mixed Type. Uncertainty analysis is given in the Supplement Sect. S2.2.

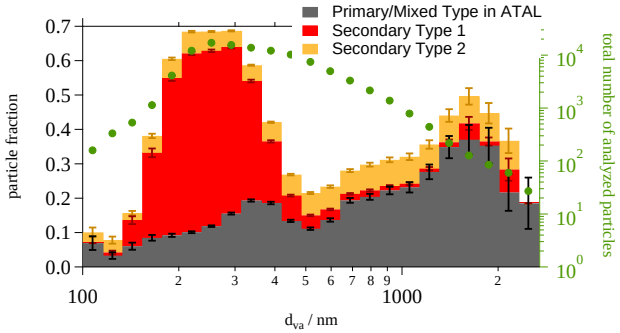

Figure 10. Size-resolved fraction of the identified particle types as measured by the ERICA-LAMS. The figure represents the cumulative particle fraction of the identified particle types: Secondary Type 1 (red) and Secondary Type 2 (orange), as well as the total number of analyzed particles per bin (dark green). The distribution of Primary/Mixed Type particles (dark grey) is limited to particles in the ATAL, thus the fractions do not add up to one. Uncertainty analysis is provided in the Sect. S2.2. This graph does not show the complete size distribution of the ambient aerosol, especially the lower cutoff is strongly influenced by the ability to detect small particles with ERICA.

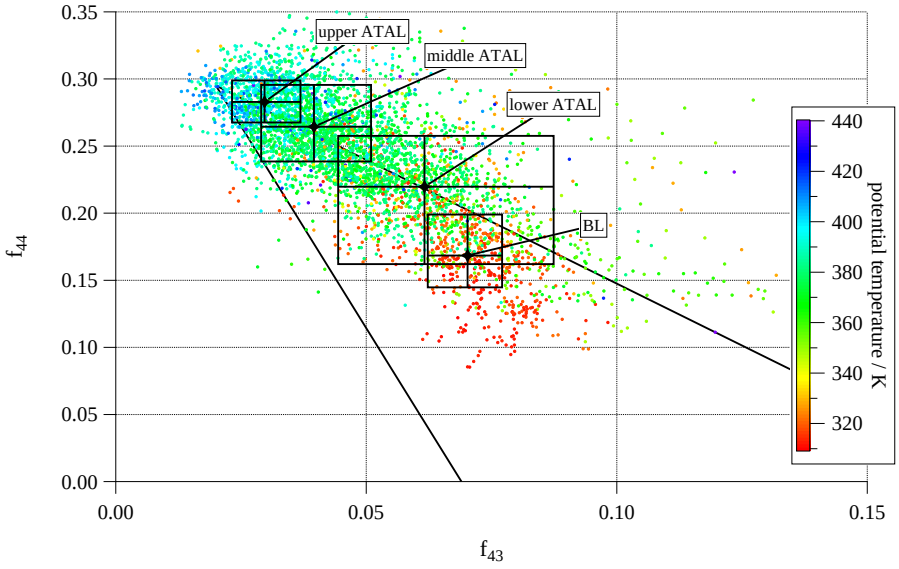

Figure 11. Graph showing the ratios f_{44} vs. f_{43} as indication for the degree of oxidation of the organic aerosol (colour coded with respect to potential temperature). Among all data points, where the total organic signal as well as the organic signals at m/z 43 and 44 are above the detection limit, we present the median values for the boundary layer ($\theta < 320$ K), the lower ATAL (355 K-370 K), the middle ATAL (370 K-390 K), and the upper ATAL (390 K-420 K) in a box representing the corresponding $25th$ and $75th$ percentiles. For the median values all data points, where organics are above the detection limit are considered. Black lines show the triangular area according to the criteria introduced by Ng et al. (2010).

~~ATAL is largely controlled by secondary formation of nitrate, ammonium, and organic aerosol, as proven by the predominance of purely secondary particles (by the ERICA-LAMS) as well as of ammonium nitrate and organics (by the ERICA-AMS).~~ Nevertheless, the abundance of potassium, iron, and elemental carbon in the mean spectrum of the primary ATAL aerosol (Fig. 8b) indicates that primary emitted BL particles, likely from biomass burning (e.g. Silva et al., 1999; Pratt et al., 2011), anthropogenic emissions (e.g. Guazzotti et al., 2003), and mineral dust (e.g. Schmidt et al., 2017), can also be transported within the AMA into the tropopause region (e.g. Hudson et al., 2004; Schill et al., 2020). In addition, the presence of iron in the primary ATAL aerosol particles (Fig. 8b) mainly originates from meteoric material that is transported from above into the upper ATAL region (Schneider et al., 2021). A detailed analysis of the measured primary particles and its vertical uplift within the AMA is subject of a follow-up study.

3.4 Measurements of particulate organosulfates

To gain further insight into the composition of secondary organic aerosol (SOA) within the ATAL, our single particle measurements by the ERICA-LAMS can be used as well. According to earlier studies, the LDI technique is able to detect the molecular identity of some organic compounds, as for example of organosulfates (OS), which are known as tracers for SOA (Froyd et al., 2010; Hatch et al., 2011a, b; Liao et al., 2015). During the StratoClim aircraft campaign 2017, we observed a significant fraction of particles containing OS in the ATAL and even in the lower stratosphere. The most abundant marker ion in the single particle spectra is given by m/z -155 ($C_2H_3O_2SO_4^-$), suggesting the presence of glyoxal sulfate or glycolic acid sulfate (GA sulfate; Froyd et al., 2010; Surratt et al., 2008; Galloway et al., 2009; Hatch et al., 2011a; Liao et al., 2015). The isotopic ratio of the m/z -155 and m/z -157 signal of 0.06 is in line with the isotopic abundance of the sulfur (and oxygen) isotopes. We found that 21 % (by number) of all analyzed particles ~~by number~~ contain GA sulfate. The mean bipolar spectra of this particle type in the stratosphere and in the ATAL are given in Fig. 12. Within the ATAL, GA sulfate is ~~largely~~to a large part internally mixed with ammonium and nitrate (Fig. 12b). Whereas in the stratosphere, GA sulfate is found on particles containing meteoric material and sulfuric acid (Fig. 12a; Schneider et al., 2021).

Figure 13 shows the vertical profile of number fraction and scaled number concentration $PF \cdot N_0$ of particles containing GA sulfate identified by a peak at m/z -155. These particles are ~~largely~~mostly present in the ATAL, particularly in the upper ATAL region. The formation of GA sulfate is dependent on the availability of precursor gases, NO_x levels above 1 ppb (Surratt et al., 2008; Froyd et al., 2010; Wennberg, 2013), and the formation of GA sulfate is enhanced at high aerosol acidity (Froyd et al., 2010). Consistently, medium to high volume mixing ratios of NO (as proxy for NO_x) were observed within the ATAL as measured by SIOUX, ranging between 0.5 and 5 ppbv with maximum values of up to 20 ppbv in very fresh convective outflow ~~(Stratmann et al., 2021)~~. Comparing Figs. 6 and 13, we can further conclude that the number fraction of particles containing GA sulfate increases with increasing aerosol acidity above 400 K (above 18 km). In line with this is the observation that the ERICA-LAMS spectra of the GA sulfate particles also concurrently exhibit ion peaks at m/z -195 and -97 ($H(HSO_4)_2^-$ and HSO_4^-, respectively), which is indicative for the presence of acidic sulfate in the single particles (Yao et al., 2011). Gas-phase organic precursors of GA sulfate are diverse and as such subject of various laboratory and modelling studies (e.g. Surratt et al.,

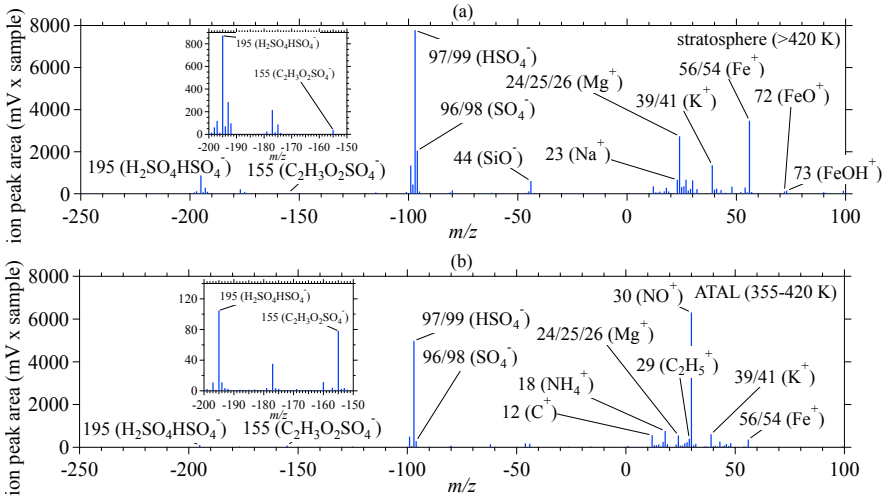

Figure 12. Bipolar mean spectra of the ERICA-LAMS particles containing organosulfates (here: glyoxal or glycolic acid sulfate evident by the abundance of m/z -155 in single particle spectra) in (a) the stratosphere above 420 K potential temperature (averaged over 2354 particles) and (b) the ATAL between 355 and 420 K (averaged over 11176 particles).

2008; Galloway et al., 2009; Schindelka et al., 2013; Liao et al., 2015; Brüggemann et al., 2020). The authors discuss glycolic acid, and methyl vinyl ketone together with their precursors (e.g. isoprene, ethene, acetic acid, acetylene, and aromatic compounds) from anthropogenic and biogenic sources as potential candidates. The mixing ratios of acetylene measured with the GLORIA instrument feature increased values in the upper troposphere and even in the lower stratosphere (Johansson et al., 2020). ~~However, such gas-phase organic precursors were not measured during the StratoClim 2017 aircraft campaign, thus we could not provide further information on the availability and identification of precursor gases to form GA sulfate.~~ In summary, we have indications that the abundance of SOA within the ATAL can be partly attributed to the formation of organosulfates in this region.

3.5 Photochemical processing of organic aerosol within the ATAL and the lower stratosphere

Particle composition in the ATAL is further influenced by photochemical processing of aerosol particles, along with the vertical uplift of air masses even reaching across the tropopause. By using the ERICA-AMS measurements, we calculated the ratio $R_{44/43}$ as the fraction of f_{44} to f_{43} to show the degree of oxidation of the organic aerosol as a function of altitude (Fig. 14; see Supplement Sect. S1.6 for further details). In the BL and lower troposphere, the ratio is relatively constant. Within the ATAL, the ratio is significantly increasing with altitude and potential temperature, demonstrating the increasing degree of oxidative ageing of organic species (Fig. 14). We thus conclude that particles formed in the lower ATAL region are further uplifted and thereby subject to extensive oxidative ageing until a potential temperature of 440 K is reached. The ensuing vertical transport of air masses above the Asian monsoon had been earlier demonstrated by several modelling studies (e.g. Pan et al., 2016;

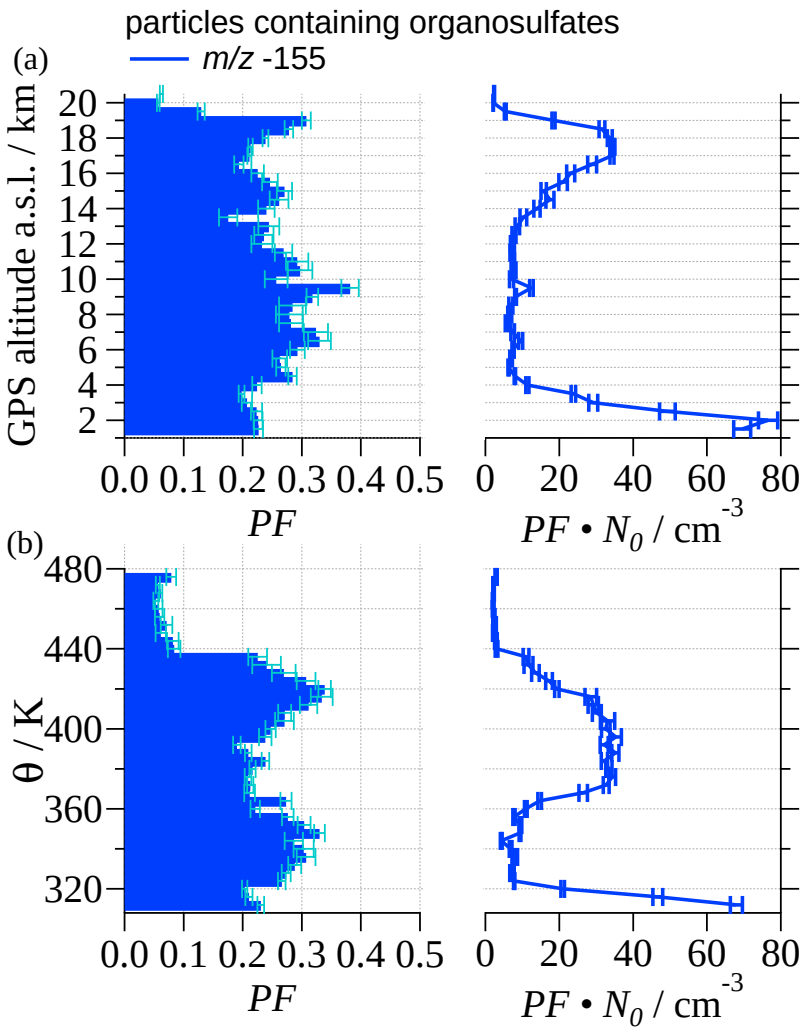

Figure 13. Vertically resolved fraction and number concentration of the particles containing organosulfates (here: glyoxal or glycolic acid sulfate evident by the abundance of m/z -155 in single particle spectra) detected by the ERICA-LAMS as a function of (a) GPS altitude and (b) potential temperature θ. The left panels represent the particle fraction (PF) of the particle type. The right panels represent the scaled ERICA-LAMS number concentrations ($PF \cdot N_0$). Uncertainty analysis is given in the Supplement Sect. S2.2.

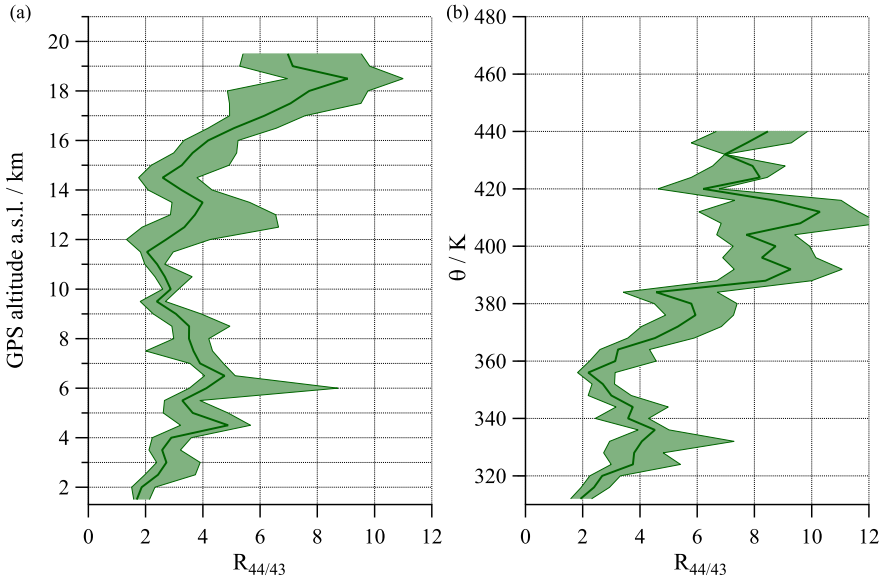

Figure 14. Vertical profiles with median and interquartile ranges of the fraction $R_{44/43}$ derived from the ERICA-AMS measurements as a function of (a) GPS altitude and (b) potential temperature θ. Values above 18.5 km or 420 K are uncertain due to low organic signals, which are very sensitive to CO_2 corrections. Only data points are shown where values of organic mass concentration as well as org44 and org43 signals are above the detection limit of the corresponding vertical bins. This condition is not fulfilled above 19 km and 440 K.

Ploeger et al., 2017; Vogel et al., 2019). Above the main convective outflow of the AMA ($\sim$360 K) radiative heating is the main process driving vertical transport until $\sim$460 K with about 1 K per day - 1.5 K per day (Ploeger et al., 2017; Vogel et al., 2019). ~~Along with the vertical uplift air inside the AMA,~~We have indications that SOA formation is ongoing in the lower stratosphere within the vertically uplifted air. At these altitudes, stratospheric background air gains in influence and mixes with the uplifted AMA air (Vogel et al., 2019). This dilution process results in decreasing concentrations of ammonium, nitrate, and organic aerosol particles. However, we observed that the mass fraction and mass concentration of organic aerosol shows a less steep decrease towards altitudes above 18 km or 420 K ~~compared to~~than for nitrate (Fig. 15 and 2). This might be explained by ongoing SOA formation above the tropopause, competing with the dilution process and in turn extending the vertical profile of organic matter towards higher altitudes compared to nitrate. This hypothesis is supported by GLORIA measurements of the precursor gases acetylene and ammonia (Johansson et al., 2020; Höpfner et al., 2019, respectively) and measurements of the precursor gas NO (Fig. 5). Observations show that acetylene and NO can reach the altitude of the tropopause and above (Fig. 2g in Johansson et al., 2020), while ammonia as precursor gas of ammonium nitrate shows enhanced concentrations at a maximum altitude of 15 km (Fig. 3d in Höpfner et al., 2019). Thus, organic precursor gases are still available even above the tropopause, while ammonia is not available in relevant concentrations. A possible explanation for the difference in the vertical distribution of acetylene and ammonia can be found in their lifetime. Ammonia reacts fast with sulfuric acid or nitric acid, whereby acetylene has a lifetime of about 2 weeks (Johansson et al., 2020).

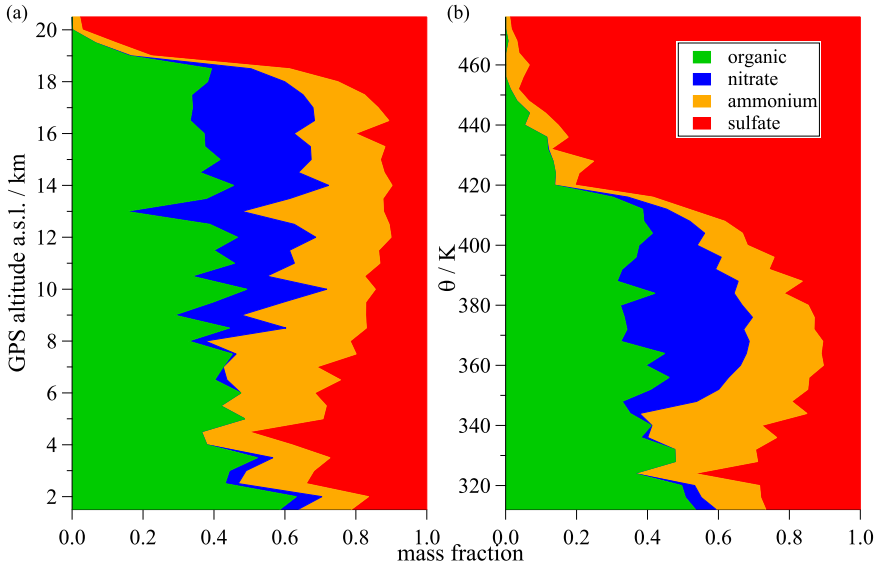

Figure 15. Vertical profiles of the cumulative mass fraction of particulate organics (green), nitrate (blue), sulfate (red), and ammonium (yellow) from the ERICA-AMS as a function of (a) GPS altitude and (b) potential temperature θ.

Consistent with this, we observed the presence of GA sulfate in the lower stratosphere, resulting in a maximum fraction of more than 30 % of the particles to contain GA sulfate at 420 K (Fig. 13). This is in line with earlier studies demonstrating that the formation of GA sulfate is supported by high aerosol acidity as found in high altitudes (Liao et al., 2015). The maximum fraction of GA sulfate containing particles at 420 K (Fig. 13) is likely formed when precursor gases from below encounter highly acidic sulfate particles from the stratosphere (Liao et al., 2015). However, the abundance of GA sulfate particles is decreasing in the lower stratosphere, which implies that the formation of GA sulfate is at a certain point also limited by the amount of gas phase precursors from below, rather than by aerosol acidity. Together, we conclude that organic aerosol in the lower stratosphere above the AMA is partly controlled by secondary formation of organosulfates that in turn is driven by the presence of stratospheric acidic aerosol and the availability of precursor gases from the AMA uplift.

4 Conclusions

The chemical nature of the ATAL has been subject of controversial discussions in the past decade. Modelling and observational (including satellites) studies provided evidence that main constituents are sulfates, organics, nitrates, and ammonium (Fadnavis et al., 2013; Neely III et al., 2014; Yu et al., 2015; Gu et al., 2016; Lelieveld et al., 2018; Fairlie et al., 2020), while others discussed the importance of mineral dust and black carbon aerosol (Fadnavis et al., 2013; Lau et al., 2018; Brühl et al., 2018; Ma et al., 2019; Yuan et al., 2019; Bossolasco et al., 2021). Motivated by the limited knowledge of chemical particle composition within the ATAL, we conducted in situ aerosol mass spectrometric measurements at high altitudes (up to 20 km or 480 K

in potential temperature) in the summertime AMA. The novel, hybrid aerosol mass spectrometer ERICA was deployed on the Russian high-altitude research aircraft M-55 *Geophysica* for eight research flights during the StratoClim field campaign based in Kathmandu, Nepal, from July 27 until August 10, 2017. The presence of the aerosol layer with increased concentrations of particulate nitrate, ammonium and organics in the altitude range between 11 km and 19 km (corresponding to ~355 K and 420 K) could be demonstrated by means of the mass spectrometric in situ measurements. The layer thus ranges from below to well above the thermal tropopause, which can be found at about 380 K. For organics, concentrations above the detection limit are found even at potential temperatures slightly higher than 420 K. The vertical profile of particulate sulfate did not exhibit a layered structure as the sulfate mass concentration increased steadily with altitude up to 20 km. The existence of the ATAL also was evident in the same altitude range from the concurrent measurements of the condensation particle counter COPAS (detecting particles larger than ~10 nm) as well as the optical particle counter UHSAS-A (for particles larger than ~65 nm). Apparently, nitrate and organics are the dominant non-refractory components of the ATAL. For both components, a concentration of around 0.8 $\mu g\,m^{-3}(NTP)$ were found as median values over the whole campaign. The organics play a comparable role to nitrate for the ATAL formation and persistence. Analyses of the concurrent availability of ammonium, nitrate, and sulfate showed that particles found up to an altitude of 18 km (~400 K) contain sufficient ammonium for completely neutralizing sulfate and nitrate. Up to 19 km (~420 K), ammonium was still detected, but not in sufficient amounts for full neutralization. However, in these analyses the possible existence of organic acids could not be considered due to the lack of suitable measurements.

Our in situ observations of particle composition ~~, including primary and secondary components,~~ show for the first time that the ATAL is largely influenced by organic and inorganic secondary aerosol formation. ~~as proven by the predominance of purely secondary particles (by the ERICA-LAMS) as well as of ammonium nitrate and organics (by the ERICA-AMS).~~ ~~Regarding secondary aerosol formation,~~ We have three main pieces of evidence. ~~prove an important role of organic and inorganic secondary aerosol formation for the particle composition in the ATAL.~~ First, by means of the LDI technique (the ERICA-LAMS), we found a dominant fraction (up to 70 % by number) of purely secondary particles particularly in the ATAL. Those particles were characterized by an internal mixture of nitrate, ammonium, sulfate, and organic matter; and as such are externally mixed with primary components (e.g. potassium and elemental carbon). Second, the size distribution of these Secondary Type particles shows lower values compared to particles containing primary components in the ATAL. Third, our observations by the ERICA-AMS show medium to high values of f_{44} (> 0.05) within the ATAL, indicating the predominance of secondary organics that have experienced oxidative ageing, rather than of fresh primary organics. Moreover, we found that organic matter in the ATAL can partly be identified by the ERICA-LAMS as organosulfates, which are known tracers for secondary organic aerosol. Particles containing glyoxal or glycolic acid sulfate (GA sulfate) show a maximum fraction in the upper ATAL region and lower stratosphere (380 - 420 K). This result might be explained by the uplift of organic precursor gases from below that encounter stratospheric acidic sulfate aerosol. The abundance of particles containing GA sulfate in the upper ATAL coincides with an increase in aerosol acidity ~~(~~ as obtained from ERICA-AMS measurements~~)~~. Consistent with this, the single particle mass spectra show an internal mixture of GA sulfate with acidic sulfate partly associated with material that can be identified as meteoric dust. Furthermore, we occasionally observed medium to high NO-regimes (> 1 ppb with maximum values of 20 ppb)

in the ATAL, which is in line with results from earlier studies on the formation of GA sulfate. We ~~showed~~demonstrated that the degree of oxidation of organic aerosol measured by the ERICA-AMS increases with altitude and potential temperature above 12 km. In particular, the measurements show that the particles in the upper ATAL and the lower stratosphere reached higher degrees of oxidation than in the lower ATAL. This indicates that particles formed in the lower ATAL are uplifted and thereby exposed to extensive oxidative ageing, consistent with earlier studies demonstrating the slow vertical uplift of AMA air in an anticyclonic spiralling range from ~ 360 K up to ~ 460 K (Ploeger et al., 2017; Vogel et al., 2019).

Inherent in the adopted experimental techniques, which rely on the detection of relatively small molecule fragments, is the well known disadvantage of not being able to unambiguously identify individual particle components (especially organic species). This is an important task for future instrumental development. Also, the data set from these eight research flights represents merely a fairly short period within only one AMA season. Further detailed in situ measurements inside the AMA are needed, especially also from the side of the Tibetan plateau.~~, which appears as exceedingly difficult considering the current geopolitical situation.~~ Also dedicated research on the processing of the aerosol and trace gases in the outflow regions of the AMA is necessary to assess the effects on radiation and cloud formation and the longer term implications of the aerosol generated within the AMA. Another open question is, how much of the aerosol actually reaches the tropical pipe entering further vertical uplift or even the stratospheric Junge layer. Taken together, our experiments provided first details on the chemical composition of the ATAL especially with respect to secondary aerosol, and the results indicate the important role of secondary organic and inorganic particle formation for the presence of the ATAL.

Data availability. The ERICA mass spectrometry data are available from the Edmond database (Edmond, 2022) and will be additionally available from the HALO database (HALO-DB) (HALO-DB, 2017) in the near future.

Author contributions. OA performed the ERICA-AMS analysis and generated the corresponding graphs, FK performed the ERICA-LAMS analysis and generated the corresponding graphs. Instrument development and operation during the campaign was done by AD, SM, OA, AH, and SB. RW and CM operated and evaluated the data of the COPAS and UHSAS-A, respectively. HS provided the NO data from SIOUX. FD and CS gave critical input for understanding and interpreting the ERICA-AMS data of the new ERICA instrument and provided help for solving instrumental issues. MP analyzed the cloud data and generated the cloud mask for data selection. FS was managing campaign operation, especially designing the flight paths to achieve the scientific goals. BV provided expertise on the Asian monsoon dynamics. The manuscript was written by SB, FK, and OA. All authors commented on the manuscript.

Competing interests. The authors declare no competing interests

Acknowledgements. The StratoClim project was funded by the EU (FP7/2007–2018 Grant No. 603557) and supported by the German Federal Ministry of Education and Research (BMBF) under the ROMIC-project SPITFIRE (01LG1205A). The work on ERICA was financed by the European Research Council under the EU's Seventh Framework Program (FP/2007-2013)/ERC Grant Agreement No.321040 ("EXCATRO") and supported by the Max Planck Society. The presented work includes contributions of the NSFC–DFG 2020 project ATAL-track (BO 1829/12-1 and VO 1276/6-1). We thank the workshops of the Max Planck Institute for Chemistry and of the Institute for Physics of the Atmosphere (Mainz University) as well as T. Böttger for building and implementing our instruments on the M-55 *Geophysica*, and Anneke M. Batenburg (now at ~~Platform Talent voor Technologie, the Hague,~~Dutch National Institute for Public Health and the Environment, Netherlands) for her valuable help during the field campaign and data collection. Also, we gratefully acknowledge Tofwerk AG (Switzerland) for their essential support, in particular M. Cubison for customizing "Tofware". Felix Plöger (IEK-7, Forschungszentrum Jülich GmbH, Jülich Germany) provided the equivalent latitude data which we gratefully acknowledge. We would like to express our gratitude to M. Rex (Alfred Wegener Institut – Helmholtz Zentrum für Polar und Meeresforschung) for managing the entire StratoClim project. We gratefully acknowledge the crew of MDB (Myasishchev Design Bureau) and the M-55 *Geophysica* pilots for their engagement and dedication. Finally, we extend our most sincere thanks to Nepalese government authorities, involved research institutions, and Tribhuvan Airport, as well as the German Embassy, for their outstanding, extraordinary support, and their fabulous hospitality that enabled our field campaign and research.

References

Andreae, M. O., Afchine, A., Albrecht, R., Holanda, B. A., Artaxo, P., Barbosa, H. M. J., Borrmann, S., Cecchini, M. A., Costa, A., Dollner, M., Fütterer, D., Järvinen, E., Jurkat, T., Klimach, T., Konemann, T., Knote, C., Krämer, M., Krisna, T., Machado, L. A. T., Mertes, S., Minikin, A., Pöhlker, C., Pöhlker, M. L., Pöschl, U., Rosenfeld, D., Sauer, D., Schlager, H., Schnaiter, M., Schneider, J., Schulz, C., Spanu, A., Sperling, V. B., Voigt, C., Walser, A., Wang, J., Weinzierl, B., Wendisch, M., and Ziereis, H.: Aerosol characteristics and particle production in the upper troposphere over the Amazon Basin, Atmospheric Chemistry and Physics, 18, 921–961, https://doi.org/10.5194/acp-18-921-2018, 2018.

Barth, M. C., Stuart, A. L., and Skamarock, W. C.: Numerical simulations of the July 10, 1996, Stratospheric-Tropospheric Experiment: Radiation, Aerosols, and Ozone (STERAO)-Deep Convection experiment storm: Redistribution of soluble tracers, Journal of Geophysical Research: Atmospheres, 106, 12 381–12 400, https://doi.org/https://doi.org/10.1029/2001JD900139, 2001.

Barth, M. C., Kim, S.-W., Skamarock, W. C., Stuart, A. L., Pickering, K. E., and Ott, L. E.: Simulations of the redistribution of formaldehyde, formic acid, and peroxides in the 10 July 1996 Stratospheric-Tropospheric Experiment: Radiation, Aerosols, and Ozone deep convection storm, Journal of Geophysical Research: Atmospheres, 112, https://doi.org/https://doi.org/10.1029/2006JD008046, 2007a.

Barth, M. C., Kim, S.-W., Wang, C., Pickering, K. E., Ott, L. E., Stenchikov, G., Leriche, M., Cautenet, S., Pinty, J.-P., Barthe, C., Mari, C., Helsdon, J. H., Farley, R. D., Fridlind, A. M., Ackerman, A. S., Spiridonov, V., and Telenta, B.: Cloud-scale model intercomparison of chemical constituent transport in deep convection, Atmospheric Chemistry and Physics, 7, 4709–4731, https://doi.org/10.5194/acp-7-4709-2007, 2007b.

Bela, M. M., Barth, M. C., Toon, O. B., Fried, A., Homeyer, C. R., Morrison, H., Cummings, K. A., Li, Y., Pickering, K. E., Allen, D. J., Yang, Q., Wennberg, P. O., Crounse, J. D., St. Clair, J. M., Teng, A. P., O'Sullivan, D., Huey, L. G., Chen, D., Liu, X., Blake, D. R., Blake, N. J., Apel, E. C., Hornbrook, R. S., Flocke, F., Campos, T., and Diskin, G.: Wet scavenging of soluble gases in DC3 deep convective storms using WRF-Chem simulations and aircraft observations, Journal of Geophysical Research: Atmospheres, 121, 4233–4257, https://doi.org/https://doi.org/10.1002/2015JD024623, 2016.

Borrmann, S., Kunkel, D., Weigel, R., Minikin, A., Deshler, T., Wilson, J. C., Curtius, J., Volk, C. M., Homan, C. D., Ulanovsky, A., Ravegnani, F., Viciani, S., Shur, G. N., Belyaev, G. V., Law, K. S., and Cairo, F.: Aerosols in the tropical and subtropical UT/LS: in-situ measurements of submicron particle abundance and volatility, Atmospheric Chemistry and Physics, 10, 5573–5592, https://doi.org/10.5194/acp-10-5573-2010, 2010.

Bossolasco, A., Jegou, F., Sellitto, P., Berthet, G., Kloss, C., and Legras, B.: Global modeling studies of composition and decadal trends of the Asian Tropopause Aerosol Layer, Atmospheric Chemistry and Physics, 21, 2745–2764, https://doi.org/10.5194/acp-21-2745-2021, 2021.

Brands, M., Kamphus, M., Böttger, T., Schneider, J., Drewnick, F., Roth, A., Curtius, J., Voigt, C., Borbon, A., Beekmann, M., Bourdon, A., Perrin, T., and Borrmann, S.: Characterization of a Newly Developed Aircraft-Based Laser Ablation Aerosol Mass Spectrometer (ALABAMA) and First Field Deployment in Urban Pollution Plumes over Paris During MEGAPOLI 2009, Aerosol Sci. Technol., 45, 46–64, https://doi.org/10.1080/02786826.2010.517813, 2011.

Brenninkmeijer, C. A. M., Crutzen, P., Boumard, F., Dauer, T., Dix, B., Ebinghaus, R., Filippi, D., Fischer, H., Franke, H., Frieβ, U., Heintzenberg, J., Helleis, F., Hermann, M., Kock, H. H., Koeppel, C., Lelieveld, J., Leuenberger, M., Martinsson, B. G., Miemczyk, S., Moret, H. P., Nguyen, H. N., Nyfeler, P., Oram, D., O'Sullivan, D., Penkett, S., Platt, U., Pupek, M., Ramonet, M., Randa, B., Reichelt, M., Rhee, T. S., Rohwer, J., Rosenfeld, K., Scharffe, D., Schlager, H., Schumann, U., Slemr, F., Sprung, D., Stock, P., Thaler, R., Valentino,

F., van Velthoven, P., Waibel, A., Wandel, A., Waschitschek, K., Wiedensohler, A., Xueref-Remy, I., Zahn, A., Zech, U., and Ziereis, H.: Civil Aircraft for the regular investigation of the atmosphere based on an instrumented container: The new CARIBIC system, Atmospheric Chemistry and Physics, 7, 4953–4976, https://doi.org/10.5194/acp-7-4953-2007, 2007.

Brühl, C., Schallock, J., Klingmüller, K., Robert, C., Bingen, C., Clarisse, L., Heckel, A., North, P., and Rieger, L.: Stratospheric aerosol radiative forcing simulated by the chemistry climate model EMAC using Aerosol CCI satellite data, Atmospheric Chemistry and Physics, 18, 12 845–12 857, https://doi.org/10.5194/acp-18-12845-2018, 2018.

Brunamonti, S., Jorge, T., Oelsner, P., Hanumanthu, S., Singh, B. B., Kumar, K. R., Sonbawne, S., Meier, S., Singh, D., Wienhold, F. G., Luo, B. P., Boettcher, M., Poltera, Y., Jauhiainen, H., Kayastha, R., Karmacharya, J., Dirksen, R., Naja, M., Rex, M., Fadnavis, S., and Peter, T.: Balloon-borne measurements of temperature, water vapor, ozone and aerosol backscatter on the southern slopes of the Himalayas during StratoClim 2016–2017, Atmospheric Chemistry and Physics, 18, 15 937–15 957, https://doi.org/10.5194/acp-18-15937-2018, 2018.

Brüggemann, M., Xu, R., Tilgner, A., Kwong, K. C., Mutzel, A., Poon, H. Y., Otto, T., Schaefer, T., Poulain, L., Chan, M. N., and Herrmann, H.: Organosulfates in Ambient Aerosol: State of Knowledge and Future Research Directions on Formation, Abundance, Fate, and Importance, Environmental Science & Technology, 54, 3767–3782, https://doi.org/10.1021/acs.est.9b06751, pMID: 32157872, 2020.

Bucci, S., Legras, B., Sellitto, P., D'Amato, F., Viciani, S., Montori, A., Chiarugi, A., Ravegnani, F., Ulanovsky, A., Cairo, F., and Stroh, F.: Deep-convective influence on the upper troposphere–lower stratosphere composition in the Asian monsoon anticyclone region: 2017 StratoClim campaign results, Atmospheric Chemistry and Physics, 20, 12 193–12 210, https://doi.org/10.5194/acp-20-12193-2020, 2020.

Canagaratna, M., Jayne, J., Jimenez, J., Allan, J., Alfarra, M., Zhang, Q., Onasch, T., Drewnick, F., Coe, H., Middlebrook, A., Delia, A., Williams, L., Trimborn, A., Northway, M., DeCarlo, P., Kolb, C., Davidovits, P., and Worsnop, D.: Chemical and microphysical characterization of ambient aerosols with the aerodyne aerosol mass spectrometer, Mass Spectrometry Reviews, 26, 185–222, https://doi.org/https://doi.org/10.1002/mas.20115, 2007.

Dragoneas, A., Molleker, S., Appel, O., Hünig, A., Böttger, T., Hermann, M., Drewnick, F., Schneider, J., Weigel, R., and Borrmann, S.: The realization of autonomous, aircraft-based, real-time aerosol mass spectrometry in the upper troposphere and lower stratosphere, EGUsphere [preprint], https://doi.org/10.5194/egusphere-2022-33, 2022.

Drewnick, F., Hings, S. S., DeCarlo, P., Jayne, J. T., Gonin, M., Fuhrer, K., Weimer, S., Jimenez, J. L., Demerjian, K. L., Borrmann, S., and Worsnop, D. R.: A New Time-of-Flight Aerosol Mass Spectrometer (TOF-AMS)—Instrument Description and First Field Deployment, Aerosol Science and Technology, 39, 637–658, https://doi.org/10.1080/02786820500182040, 2005.

Drewnick, F., Hings, S. S., Alfarra, M. R., Prevot, A. S. H., and Borrmann, S.: Aerosol quantification with the Aerodyne Aerosol Mass Spectrometer: detection limits and ionizer background effects, Atmospheric Measurement Techniques, 2, 33–46, https://doi.org/10.5194/amt-2-33-2009, 2009.

Edmond: ERICA-MS-Data StratoClim2017, https://doi.org/10.17617/3.8x, 2022.

Fadnavis, S., Semeniuk, K., Pozzoli, L., Schultz, M. G., Ghude, S. D., Das, S., and Kakatkar, R.: Transport of aerosols into the UTLS and their impact on the Asian monsoon region as seen in a global model simulation, Atmospheric Chemistry and Physics, 13, 8771–8786, https://doi.org/10.5194/acp-13-8771-2013, 2013.

Fadnavis, S., Roy, C., Chattopadhyay, R., Sioris, C. E., Rap, A., Müller, R., Kumar, K. R., and Krishnan, R.: Transport of trace gases via eddy shedding from the Asian summer monsoon anticyclone and associated impacts on ozone heating rates, Atmospheric Chemistry and Physics, 18, 11 493–11 506, https://doi.org/10.5194/acp-18-11493-2018, 2018.

Fadnavis, S., Sabin, T. P., Roy, C., Rowlinson, M., Rap, A., Vernier, J.-P., and Sioris, C. E.: Elevated aerosol layer over South Asia worsens the Indian droughts, Scientific Reports, 9, https://doi.org/10.1038/s41598-019-46704-9, 2019.

Fairlie, T. D., Liu, H., Vernier, J.-P., Campuzano-Jost, P., Jimenez, J. L., Jo, D. S., Zhang, B., Natarajan, M., Avery, M. A., and Huey, G.: Estimates of Regional Source Contributions to the Asian Tropopause Aerosol Layer Using a Chemical Transport Model, Journal of Geophysical Research: Atmospheres, 125, e2019JD031 506, https://doi.org/https://doi.org/10.1029/2019JD031506, e2019JD031506 2019JD031506, 2020.

Froyd, K. D., Murphy, S. M., Murphy, D. M., de Gouw, J. A., Eddingsaas, N. C., and Wennberg, P. O.: Contribution of isoprene-derived organosulfates to free tropospheric aerosol mass, P. Natl. Acad. Sci., 107, 21 360–21 365, https://doi.org/10.1073/pnas.1012561107, 2010.

Fujiwara, M., Sakai, T., Nagai, T., Shiraishi, K., Inai, Y., Khaykin, S., Xi, H., Shibata, T., Shiotani, M., and Pan, L. L.: Lower-stratospheric aerosol measurements in eastward-shedding vortices over Japan from the Asian summer monsoon anticyclone during the summer of 2018, Atmospheric Chemistry and Physics, 21, 3073–3090, https://doi.org/10.5194/acp-21-3073-2021, 2021.

Galloway, M. M., Chhabra, P. S., Chan, A. W. H., Surratt, J. D., Flagan, R. C., Seinfeld, J. H., and Keutsch, F. N.: Glyoxal uptake on ammonium sulphate seed aerosol: reaction products and reversibility of uptake under dark and irradiated conditions, Atmospheric Chemistry and Physics, 9, 3331–3345, https://doi.org/10.5194/acp-9-3331-2009, 2009.

Garny, H. and Randel, W. J.: Transport pathways from the Asian monsoon anticyclone to the stratosphere, Atmospheric Chemistry and Physics, 16, 2703–2718, https://doi.org/10.5194/acp-16-2703-2016, 2016.

Ge, C., Zhu, C., Francisco, J. S., Zeng, X. C., and Wang, J.: A molecular perspective for global modeling of upper atmospheric NH3 from freezing clouds, Proceedings of the National Academy of Sciences, 115, 6147–6152, https://doi.org/10.1073/pnas.1719949115, 2018.

Gu, Y., Liao, H., and Bian, J.: Summertime nitrate aerosol in the upper troposphere and lower stratosphere over the Tibetan Plateau and the South Asian summer monsoon region, Atmospheric Chemistry and Physics, 16, 6641–6663, https://doi.org/10.5194/acp-16-6641-2016, 2016.

Guazzotti, S. A., Suess, D. T., Coffee, K. R., Quinn, P. K., Bates, T. S., Wisthaler, A., Hansel, A., Ball, W. P., Dickerson, R. R., Neusüß, C., Crutzen, P. J., and Prather, K. A.: Characterization of carbonaceous aerosols outflow from India and Arabia: Biomass/biofuel burning and fossil fuel combustion, J. Geophys. Res.-Atmos., 108, https://doi.org/10.1029/2002JD003277, 2003.

HALO-DB: Mission: STRATOCLIM, https://halo-db.pa.op.dlr.de/mission/101, dataset 8540-8563, 2017.

Hanumanthu, S., Vogel, B., Müller, R., Brunamonti, S., Fadnavis, S., Li, D., Ölsner, P., Naja, M., Singh, B. B., Kumar, K. R., Sonbawne, S., Jauhiainen, H., Vömel, H., Luo, B., Jorge, T., Wienhold, F. G., Dirkson, R., and Peter, T.: Strong day-to-day variability of the Asian Tropopause Aerosol Layer (ATAL) in August 2016 at the Himalayan foothills, Atmospheric Chemistry and Physics, 20, 14 273–14 302, https://doi.org/10.5194/acp-20-14273-2020, 2020.

Hatch, L. E., Creamean, J. M., Ault, A. P., Surratt, J. D., Chan, M. N., Seinfeld, J. H., Edgerton, E. S., Su, Y., and Prather, K. A.: Measurements of Isoprene-Derived Organosulfates in Ambient Aerosol by Aerosol Time-of-Flight Mass Spectrometry - Part 1: Single Particle Atmospheric Observations in Atlanta, Environ. Sci. Technol., 40, 8648–8655, https://doi.org/10.1021/es2011836, 2011a.

Hatch, L. E., Creamean, J. M., Ault, A. P., Surratt, J. D., Chan, M. N., Seinfeld, J. H., Edgerton, E. S., Su, Y., and Prather, K. A.: Measurements of Isoprene-Derived Organosulfates in Ambient Aerosols by Aerosol Time-of-Flight Mass Spectrometry—Part 2: Temporal Variability and Formation Mechanisms, Environmental Science & Technology, 45, 8648–8655, https://doi.org/10.1021/es2011836, pMID: 21905661, 2011b.

Hinz, K. P., Greweling, M., Drews, F., and Spengler, B.: Data processing in on-line laser mass spectrometry of inorganic, organic, or biological airborne particles, J. Am. Soc. Mass Spectrom., 10, 648–660, https://doi.org/10.1016/S1044-0305(99)00028-8, 1999.

Hock, N., Schneider, J., Borrmann, S., Römpp, A., Moortgat, G., Franze, T., Schauer, C., Pöschl, U., Plass-Dülmer, C., and Berresheim, H.: Rural continental aerosol properties and processes observed during the Hohenpeissenberg Aerosol Characterization Experiment (HAZE2002), Atmospheric Chemistry and Physics, 8, 603–623, https://doi.org/10.5194/acp-8-603-2008, 2008.

Hoog, I., Mitra, S. K., Diehl, K., and Borrmann, S.: Laboratory studies about the interaction of ammonia with ice crystals at temperatures between 0 and -20°C, Journal of Atmospheric Chemistry, 57, 73–84, https://doi.org/10.1007/s10874-007-9063-0, 2007.

Hudson, P. K., Murphy, D. M., Cziczo, D. J., Thomson, D. S., de Gouw, J. A., Warneke, C., Holloway, J., Jost, H.-J., and Hübler, G.: Biomass-burning particle measurements: Characteristic composition and chemical processing, J. Geophys. Res., 109, https://doi.org/10.1029/2003JD004398, 2004.

Hünig, A., Appel, O., Dragoneas, A., Molleker, S., Clemen, H.-C., Helleis, F., Klimach, T., Köllner, F., Böttger, T., Drewnick, F., Schneider, J., and Borrmann, S.: Design, characterization, and first field deployment of a novel aircraft-based aerosol mass spectrometer combining the laser ablation and flash vaporization techniques, Atmospheric Measurement Techniques, 15, 2889–2921, https://doi.org/10.5194/amt-15-2889-2022, 2022.

Höpfner, M., Volkamer, R., Grabowski, U., Grutter, M., Orphal, J., Stiller, G., von Clarmann, T., and Wetzel, G.: First detection of ammonia (NH_3) in the Asian summer monsoon upper troposphere, Atmospheric Chemistry and Physics, 16, 14 357–14 369, https://doi.org/10.5194/acp-16-14357-2016, 2016.

Höpfner, M., Ungermann, J., Borrmann, S., Wagner, R., Spang, R., Riese, M., Stiller, G., Appel, O., Batenburg, A. M., Bucci, S., Cairo, F., Dragoneas, A., Friedl-Vallon, F., Hünig, A., Johansson, S., Krasauskas, L., Legras, B., Leisner, T., Mahnke, C., Möhler, O., Molleker, S., Müller, R., Neubert, T., Orphal, J., Preusse, P., Rex, M., Saathoff, H., Stroh, F., Weigel, R., and Wohltmann, I.: Ammonium nitrate particles formed in upper troposphere from ground ammonia sources during Asian monsoons, Nature Geoscience, 12, 608–612, https://doi.org/10.1038/s41561-019-0385-8, 2019.

Jimenez, J. L., Canagaratna, M. R., Donahue, N. M., Prevot, A. S. H., Zhang, Q., Kroll, J. H., DeCarlo, P. F., Allan, J. D., Coe, H., Ng, N. L., Aiken, A. C., Docherty, K. S., Ulbrich, I. M., Grieshop, A. P., Robinson, A. L., Duplissy, J., Smith, J. D., Wilson, K. R., Lanz, V. A., Hueglin, C., Sun, Y. L., Tian, J., Laaksonen, A., Raatikainen, T., Rautiainen, J., Vaattovaara, P., Ehn, M., Kulmala, M., Tomlinson, J. M., Collins, D. R., Cubison, M. J., Dunlea, E. J., Huffman, J. A., Onasch, T. B., Alfarra, M. R., Williams, P. I., Bower, K., Kondo, Y., Schneider, J., Drewnick, F., Borrmann, S., Weimer, S., Demerjian, K., Salcedo, D., Cottrell, L., Griffin, R., Takami, A., Miyoshi, T., Hatakeyama, S., Shimono, A., Sun, J. Y., Zhang, Y. M., Dzepina, K., Kimmel, J. R., Sueper, D., Jayne, J. T., Herndon, S. C., Trimborn, A. M., Williams, L. R., Wood, E. C., Middlebrook, A. M., Kolb, C. E., Baltensperger, U., and Worsnop, D. R.: Evolution of Organic Aerosols in the Atmosphere, Science, 326, 1525–1529, https://doi.org/10.1126/science.1180353, 2009.

Johansson, S., Höpfner, M., Kirner, O., Wohltmann, I., Bucci, S., Legras, B., Friedl-Vallon, F., Glatthor, N., Kretschmer, E., Ungermann, J., and Wetzel, G.: Pollution trace gas distributions and their transport in the Asian monsoon upper troposphere and lowermost stratosphere during the StratoClim campaign 2017, Atmospheric Chemistry and Physics, 20, 14 695–14 715, https://doi.org/10.5194/acp-20-14695-2020, 2020.

Jost, A., Szakáll, M., Diehl, K., Mitra, S. K., and Borrmann, S.: Chemistry of riming: the retention of organic and inorganic atmospheric trace constituents, Atmospheric Chemistry and Physics, 17, 9717–9732, https://doi.org/10.5194/acp-17-9717-2017, 2017.

Kane, D. B., Oktem, B., and Johnston, M. V.: Nanoparticle Detection by Aerosol Mass Spectrometry, Aerosol Sci. Technol., 34, 520–527, https://doi.org/10.1080/02786820117085, 2001.

Klimach, T.: Chemische Zusammensetzung der Aerosole: Design und Datenauswertung eines Einzelpartikel-Laserablationsmassenspektrometers, Ph.D. thesis, Johannes-Gutenberg Universität Mainz, 2012.

Köllner, F., Schneider, J., Willis, M. D., Klimach, T., Helleis, F., Bozem, H., Kunkel, D., Hoor, P., Burkart, J., Leaitch, W. R., Aliabadi, A. A., Abbatt, J. P. D., Herber, A. B., and Borrmann, S.: Particulate trimethylamine in the summertime Canadian high Arctic lower troposphere, Atmos. Chem. Phys., 17, 13 747–13 766, https://doi.org/10.5194/acp-17-13747-2017, 2017.

Köllner, F., Schneider, J., Willis, M. D., Schulz, H., Kunkel, D., Bozem, H., Hoor, P., Klimach, T., Helleis, F., Burkart, J., Leaitch, W. R., Aliabadi, A. A., Abbatt, J. P. D., Herber, A. B., and Borrmann, S.: Chemical composition and source attribution of sub-micrometre aerosol particles in the summertime Arctic lower troposphere, Atmospheric Chemistry and Physics, 21, 6509–6539, https://doi.org/10.5194/acp-21-6509-2021, 2021.

Lau, W. K. M., Yuan, C., and Li, Z.: Origin, Maintenance and Variability of the Asian Tropopause Aerosol Layer (ATAL): The Roles of Monsoon Dynamics, Sci Rep, 8, 3960, https://doi.org/10.1038/s41598-018-22267-z, 2018.

Lawrence, M. G. and Lelieveld, J.: Atmospheric pollutant outflow from southern Asia: a review, Atmospheric Chemistry and Physics, 10, 11 017–11 096, https://doi.org/10.5194/acp-10-11017-2010, 2010.

Lelieveld, J., Bourtsoukidis, E., Brühl, C., Fischer, H., Fuchs, H., Harder, H., Hofzumahaus, A., Holland, F., Marno, D., Neumaier, M., Pozzer, A., Schlager, H., Williams, J., Zahn, A., and Ziereis, H.: The South Asian monsoon—pollution pump and purifier, Science, 361, 270–273, https://doi.org/10.1126/science.aar2501, 2018.

Liao, J., Froyd, K. D., Murphy, D. M., Keutsch, F. N., Yu, G., Wennberg, P. O., St. Clair, J. M., Crounse, J. D., Wisthaler, A., Mikoviny, T., Jimenez, J. L., Campuzano-Jost, P., Day, D. A., Hu, W., Ryerson, T. B., Pollack, I. B., Peischl, J., Anderson, B. E., Ziemba, L. D., Blake, D. R., Meinardi, S., and Diskin, G.: Airborne measurements of organosulfates over the continental U.S., Journal of Geophysical Research: Atmospheres, 120, 2990–3005, https://doi.org/https://doi.org/10.1002/2014JD022378, 2015.

Liu, X., Penner, J. E., and Wang, M.: Influence of anthropogenic sulfate and black carbon on upper tropospheric clouds in the NCAR CAM3 model coupled to the IMPACT global aerosol model, Journal of Geophysical Research, 114, https://doi.org/10.1029/2008JD010492, 2009.

Ma, J., Brühl, C., He, Q., Steil, B., Karydis, V. A., Klingmüller, K., Tost, H., Chen, B., Jin, Y., Liu, N., Xu, X., Yan, P., Zhou, X., Abdelrahman, K., Pozzer, A., and Lelieveld, J.: Modeling the aerosol chemical composition of the tropopause over the Tibetan Plateau during the Asian summer monsoon, Atmospheric Chemistry and Physics, 19, 11 587–11 612, https://doi.org/10.5194/acp-19-11587-2019, 2019.

Mahnke, C., Weigel, R., Cairo, F., Vernier, J.-P., Afchine, A., Krämer, M., Mitev, V., Matthey, R., Viciani, S., D'Amato, F., Ploeger, F., Deshler, T., and Borrmann, S.: The Asian tropopause aerosol layer within the 2017 monsoon anticyclone: microphysical properties derived from aircraft-borne in situ measurements, Atmospheric Chemistry and Physics, 21, 15 259–15 282, https://doi.org/10.5194/acp-21-15259-2021, 2021.

Metzger, S., Dentener, F., Krol, M., Jeuken, A., and Lelieveld, J.: Gas/aerosol partitioning 2. Global modeling results, Journal of Geophysical Research: Atmospheres, 107, ACH 17–1–ACH 17–23, https://doi.org/https://doi.org/10.1029/2001JD001103, 2002.

Moffet, R. C. and Prather, K. A.: In-situ measurements of the mixing state and optical properties of soot with implications for radiative forcing estimates, P. Natl. Acad. Sci., 106, 11 872–11 877, https://doi.org/10.1073/pnas.0900040106, 2009.

Molleker, S., Helleis, F., Klimach, T., Appel, O., Clemen, H.-C., Dragoneas, A., Gurk, C., Hünig, A., Köllner, F., Rubach, F., Schulz, C., Schneider, J., and Borrmann, S.: Application of an O-ring pinch device as a constant-pressure inlet (CPI) for airborne sampling, Atmospheric Measurement Techniques, 13, 3651–3660, https://doi.org/10.5194/amt-13-3651-2020, 2020.

Murphy, D. M.: The design of single particle laser mass spectrometers, Mass Spectrometry Reviews, 26, 150–165, https://doi.org/https://doi.org/10.1002/mas.20113, 2007.

Murphy, D. M., Froyd, K. D., Schwarz, J. P., and Wilson, J. C.: Observations of the chemical composition of stratospheric aerosol particles, Quarterly Journal of the Royal Meteorological Society, 140, 1269–1278, https://doi.org/https://doi.org/10.1002/qj.2213, 2014.

Neely III, R. R., Yu, P., Rosenlof, K. H., Toon, O. B., Daniel, J. S., Solomon, S., and Miller, H. L.: The contribution of anthropogenic SO2 emissions to the Asian tropopause aerosol layer, Journal of Geophysical Research: Atmospheres, 119, 1571–1579, https://doi.org/https://doi.org/10.1002/2013JD020578, 2014.

Ng, N. L., Canagaratna, M. R., Zhang, Q., Jimenez, J. L., Tian, J., Ulbrich, I. M., Kroll, J. H., Docherty, K. S., Chhabra, P. S., Bahreini, R., Murphy, S. M., Seinfeld, J. H., Hildebrandt, L., Donahue, N. M., DeCarlo, P. F., Lanz, V. A., Prévôt, A. S. H., Dinar, E., Rudich, Y., and Worsnop, D. R.: Organic aerosol components observed in Northern Hemispheric datasets from Aerosol Mass Spectrometry, Atmospheric Chemistry and Physics, 10, 4625–4641, https://doi.org/10.5194/acp-10-4625-2010, 2010.

Ng, N. L., Canagaratna, M. R., Jimenez, J. L., Chhabra, P. S., Seinfeld, J. H., and Worsnop, D. R.: Changes in organic aerosol composition with aging inferred from aerosol mass spectra, Atmos. Chem. Phys., 11, 6465–6474, https://doi.org/10.5194/acp-11-6465-2011, 2011.

Nützel, M., Dameris, M., and Garny, H.: Movement, drivers and bimodality of the South Asian High, Atmospheric Chemistry and Physics, 16, 14 755–14 774, https://doi.org/10.5194/acp-16-14755-2016, 2016.

Pan, L. L., Honomichl, S. B., Kinnison, D. E., Abalos, M., Randel, W. J., Bergman, J. W., and Bian, J.: Transport of chemical tracers from the boundary layer to stratosphere associated with the dynamics of the Asian summer monsoon, Journal of Geophysical Research: Atmospheres, 121, 14,159–14,174, https://doi.org/10.1002/2016jd025616, 2016.

Park, M., Randel, W. J., Emmons, L. K., and Livesey, N. J.: Transport pathways of carbon monoxide in the Asian summer monsoon diagnosed from Model of Ozone and Related Tracers (MOZART), Journal of Geophysical Research: Atmospheres, 114, https://doi.org/https://doi.org/10.1029/2008JD010621, 2009.

Peck, J., Gonzalez, L. A., Williams, L. R., Xu, W., Croteau, P. L., Timko, M. T., Jayne, J. T., Worsnop, D. R., Miake-Lye, R. C., and Smith, K. A.: Development of an aerosol mass spectrometer lens system for PM2.5, Aerosol Science and Technology, 50, 781–789, https://doi.org/10.1080/02786826.2016.1190444, 2016.

Ploeger, F., Gottschling, C., Griessbach, S., Grooß, J.-U., Guenther, G., Konopka, P., Müller, R., Riese, M., Stroh, F., Tao, M., Ungermann, J., Vogel, B., and von Hobe, M.: A potential vorticity-based determination of the transport barrier in the Asian summer monsoon anticyclone, Atmospheric Chemistry and Physics, 15, 13 145–13 159, https://doi.org/10.5194/acp-15-13145-2015, 2015.

Ploeger, F., Konopka, P., Walker, K., and Riese, M.: Quantifying pollution transport from the Asian monsoon anticyclone into the lower stratosphere, Atmospheric Chemistry and Physics, 17, 7055–7066, https://doi.org/10.5194/acp-17-7055-2017, 2017.

Popovic, J. M. and Plumb, R. A.: Eddy Shedding from the Upper-Tropospheric Asian Monsoon Anticyclone, Journal of the Atmospheric Sciences, 58, 93 – 104, https://doi.org/10.1175/1520-0469(2001)058<0093:ESFTUT>2.0.CO;2, 2001.

Pratt, K. A., Murphy, S. M., Subramanian, R., DeMott, P. J., Kok, G. L., Campos, T., Rogers, D. C., Prenni, A. J., Heymsfield, A. J., Seinfeld, J. H., and Prather, K. A.: Flight-based chemical characterization of biomass burning aerosols within two prescribed burn smoke plumes, Atmos. Chem. Phys., 11, 12 549–12 565, https://doi.org/10.5194/acp-11-12549-2011, 2011.

Randel, W. and Jensen, E.: Physical processes in the tropical tropopause layer and their roles in a changing climate, Nature Geosci, 6, https://doi.org/10.1038/ngeo1733, 2013.

Randel, W. J. and Park, M.: Deep convective influence on the Asian summer monsoon anticyclone and associated tracer variability observed with Atmospheric Infrared Sounder (AIRS), Journal of Geophysical Research: Atmospheres, 111, https://doi.org/https://doi.org/10.1029/2005JD006490, 2006.

Randel, W. J., Park, M., Emmons, L., Kinnison, D., Bernath, P., Walker, K. A., Boone, C., and Pumphrey, H.: Asian Monsoon Transport of Pollution to the Stratosphere, Science, 328, 611–613, https://doi.org/10.1126/science.1182274, 2010.

Reitz, P.: Chemical composition measurements of cloud condensation nuclei and ice nuclei by aerosol mass spectrometry, Ph.D. thesis, Johannes Gutenberg-Universität Mainz, 2011.

Ridley, D. A., Solomon, S., Barnes, J. E., Burlakov, V. D., Deshler, T., Dolgii, S. I., Herber, A. B., Nagai, T., Neely III, R. R., Nevzorov, A. V., Ritter, C., Sakai, T., Santer, B. D., Sato, M., Schmidt, A., Uchino, O., and Vernier, J. P.: Total volcanic stratospheric aerosol optical depths and implications for global climate change, Geophysical Research Letters, 41, 7763–7769, https://doi.org/https://doi.org/10.1002/2014GL061541, 2014.

Roth, A., Schneider, J., Klimach, T., Mertes, S., van Pinxteren, D., Herrmann, H., and Borrmann, S.: Aerosol properties, source identification, and cloud processing in orographic clouds measured by single particle mass spectrometry on a central European mountain site during HCCT-2010, Atmos. Chem. Phys., 16, 505–524, https://doi.org/10.5194/acp-16-505-2016, 2016.

Savitzky, A. and Golay, M. J. E.: Smoothing and Differentiation of Data by Simplified Least Squares Procedures, Analytical Chemistry, 36, 1627–1639, https://doi.org/10.1021/ac60214a047, 1964.

Schill, G. P., Froyd, K. D., Bian, H., Kupc, A., Williamson, C., Brock, C. A., Ray, E., Hornbrook, R. S., Hills, A. J., Apel, E. C., Chin, M., Colarco, P. R., and Murphy, D. M.: Widespread biomass burning smoke throughout the remote troposphere, Nature Geoscience, 13, 422–427, https://doi.org/10.1038/s41561-020-0586-1, 2020.

Schindelka, J., Iinuma, Y., Hoffmann, D., and Herrmann, H.: Sulfate radical-initiated formation of isoprene-derived organosulfates in atmospheric aerosols, Faraday Discuss., 165, 237–259, https://doi.org/10.1039/C3FD00042G, 2013.

Schmidt, S., Schneider, J., Klimach, T., Mertes, S., Schenk, L. P., Kupiszewski, P., Curtius, J., and Borrmann, S.: Online single particle analysis of ice particle residuals from mountain-top mixed-phase clouds using laboratory derived particle type assignment, Atmos. Chem. Phys., 17, 575–594, https://doi.org/10.5194/acp-17-575-2017, 2017.

Schneider, J., Weigel, R., Klimach, T., Dragoneas, A., Appel, O., Hünig, A., Molleker, S., Köllner, F., Clemen, H.-C., Eppers, O., Hoppe, P., Hoor, P., Mahnke, C., Krämer, M., Rolf, C., Grooß, J.-U., Zahn, A., Obersteiner, F., Ravegnani, F., Ulanovsky, A., Schlager, H., Scheibe, M., Diskin, G. S., DiGangi, J. P., Nowak, J. B., Zöger, M., and Borrmann, S.: Aircraft-based observation of meteoric material in lower-stratospheric aerosol particles between 15 and 68° N, Atmospheric Chemistry and Physics, 21, 989–1013, https://doi.org/10.5194/acp-21-989-2021, 2021.

Schulz, C., Schneider, J., Amorim Holanda, B., Appel, O., Costa, A., de Sá, S. S., Dreiling, V., Fütterer, D., Jurkat-Witschas, T., Klimach, T., Knote, C., Krämer, M., Martin, S. T., Mertes, S., Pöhlker, M. L., Sauer, D., Voigt, C., Walser, A., Weinzierl, B., Ziereis, H., Zöger, M., Andreae, M. O., Artaxo, P., Machado, L. A. T., Pöschl, U., Wendisch, M., and Borrmann, S.: Aircraft-based observations of isoprene-epoxydiol-derived secondary organic aerosol (IEPOX-SOA) in the tropical upper troposphere over the Amazon region, Atmospheric Chemistry and Physics, 18, 14 979–15 001, https://doi.org/10.5194/acp-18-14979-2018, 2018.

Silva, P. J. and Prather, K. A.: Interpretation of Mass Spectra from Organic Compounds in Aerosol Time-of-Flight Mass Spectrometry, Anal. Chem., 72, 3553–3562, https://doi.org/10.1021/ac9910132, 2000.

Silva, P. J., Liu, D.-Y., Noble, C. A., and Prather, K. A.: Size and Chemical Characterization of Individual Particles Resulting from Biomass Burning of Local Southern California Species, Environ. Sci. Technol., 33, 3068–3076, https://doi.org/10.1021/es980544p, 1999.

Sokolov, L. and Lepuchov, B.: Protocol of interaction between Unit for Connection with Scientific Equipment (UCSE) and on-board scientific equipment of Geophysica aircraft, Tech. rep., Myasishchev Design Bureau (MDB), 1998.

Stratmann, G., Ziereis, H., Stock, P., Brenninkmeijer, C., Zahn, A., Rauthe-Schöch, A., Velthoven, P., Schlager, H., and Volz-Thomas, A.: NO and NOy in the upper troposphere: Nine years of CARIBIC measurements onboard a passenger aircraft, Atmospheric Environment, 133, https://doi.org/10.1016/j.atmosenv.2016.02.035, 2016.

Stratmann, G., Schlager, H., Mertens, M., Nuetzel, N., Heuchert, J., Rieger, V., and Jöckel, P.: First Measurements of Nitrogen Monoxide in the Center of the Asian Summer Monsoon Anticyclone from the High-Altitude Research Aircraft Geophysica and Accompanying Model Simulations, submitted to GLR, 2021.

Suess, D. T. and Prather, K. A.: Mass Spectrometry of Aerosols, Chem. Rev., 99, 3007–3036, https://doi.org/10.1021/cr980138o, 1999.

Surratt, J. D., Gómez-González, Y., Chan, A. W. H., Vermeylen, R., Shahgholi, M., Kleindienst, T. E., Edney, E. O., Offenberg, J. H., Lewandowski, M., Jaoui, M., Maenhaut, W., Claeys, M., Flagan, R. C., and Seinfeld, J. H.: Organosulfate Formation in Biogenic Secondary Organic Aerosol, The Journal of Physical Chemistry A, 112, 8345–8378, https://doi.org/10.1021/jp802310p, pMID: 18710205, 2008.

Talukdar, R. K., Burkholder, J. B., Roberts, J. M., Portmann, R. W., and Ravishankara, A. R.: Heterogeneous Interaction of N2O5 with HCl Doped H2SO4 under Stratospheric Conditions: ClNO2 and Cl2 Yields, The Journal of Physical Chemistry A, 116, 6003–6014, https://doi.org/10.1021/jp210960z, pMID: 22268510, 2012.

Thomason, L. W. and Vernier, J.-P.: Improved SAGE II cloud/aerosol categorization and observations of the Asian tropopause aerosol layer: 1989–2005, Atmospheric Chemistry and Physics, 13, 4605–4616, https://doi.org/10.5194/acp-13-4605-2013, 2013.

Thomson, D. S., Middlebrook, A. M., and Murphy, D. M.: Thresholds for Laser-Induced Ion Formation from Aerosols in a Vacuum Using Ultraviolet and Vacuum-Ultraviolet Laser Wavelengths, Aerosol Sci. Technol., 26, 544–559, https://doi.org/10.1080/02786829708965452, 1997.

Tost, H.: Chemistry–climate interactions of aerosol nitrate from lightning, Atmospheric Chemistry and Physics, 17, 1125–1142, https://doi.org/10.5194/acp-17-1125-2017, 2017.

Tost, H., Lawrence, M. G., Brühl, C., Jöckel, P., Team, T. G., and Team, T. S.-O.-D.: Uncertainties in atmospheric chemistry modelling due to convection parameterisations and subsequent scavenging, Atmospheric Chemistry and Physics, 10, 1931–1951, https://doi.org/10.5194/acp-10-1931-2010, 2010.

Ueyama, R., Jensen, E. J., and Pfister, L.: Convective Influence on the Humidity and Clouds in the Tropical Tropopause Layer During Boreal Summer, Journal of Geophysical Research: Atmospheres, 123, 7576–7593, https://doi.org/https://doi.org/10.1029/2018JD028674, 2018.

Vernier, J. P., Pommereau, J. P., Garnier, A., Pelon, J., Larsen, N., Nielsen, J., Christensen, T., Cairo, F., Thomason, L. W., Leblanc, T., and McDermid, I. S.: Tropical stratospheric aerosol layer from CALIPSO lidar observations, Journal of Geophysical Research: Atmospheres, 114, https://doi.org/https://doi.org/10.1029/2009JD011946, 2009.

Vernier, J.-P., Thomason, L. W., and Kar, J.: CALIPSO detection of an Asian tropopause aerosol layer, Geophysical Research Letters, 38, https://doi.org/https://doi.org/10.1029/2010GL046614, 2011.

Vernier, J.-P., Fairlie, T. D., Natarajan, M., Wienhold, F. G., Bian, J., Martinsson, B. G., Crumeyrolle, S., Thomason, L. W., and Bedka, K. M.: Increase in upper tropospheric and lower stratospheric aerosol levels and its potential connection with Asian pollution, Journal of Geophysical Research: Atmospheres, 120, 1608–1619, https://doi.org/https://doi.org/10.1002/2014JD022372, 2015.

Vernier, J.-P., Fairlie, T. D., Deshler, T., Ratnam, M. V., Gadhavi, H., Kumar, B. S., Natarajan, M., Pandit, A. K., Raj, S. T. A., Kumar, A. H., Jayaraman, A., Singh, A. K., Rastogi, N., Sinha, P. R., Kumar, S., Tiwari, S., Wegner, T., Baker, N., Vignelles, D., Stenchikov, G., Shevchenko, I., Smith, J., Bedka, K., Kesarkar, A., Singh, V., Bhate, J., Ravikiran, V., Rao, M. D., Ravindrababu, S., Patel, A., Vernier, H., Wienhold, F. G., Liu, H., Knepp, T. N., Thomason, L., Crawford, J., Ziemba, L., Moore, J., Crumeyrolle, S., Williamson, M., Berthet, G., Jégou, F., and Renard, J.-B.: BATAL: The Balloon Measurement Campaigns of the Asian Tropopause Aerosol Layer, Bulletin of the American Meteorological Society, 99, 955 – 973, https://doi.org/10.1175/BAMS-D-17-0014.1, 2018.

Vogel, B., Günther, G., Müller, R., Grooß, J.-U., Hoor, P., Krämer, M., Müller, S., Zahn, A., and Riese, M.: Fast transport from Southeast Asia boundary layer sources to northern Europe: rapid uplift in typhoons and eastward eddy shedding of the Asian monsoon anticyclone, Atmospheric Chemistry and Physics, 14, 12 745–12 762, https://doi.org/10.5194/acp-14-12745-2014, 2014.

Vogel, B., Günther, G., Müller, R., Grooß, J.-U., and Riese, M.: Impact of different Asian source regions on the composition of the Asian monsoon anticyclone and of the extratropical lowermost stratosphere, Atmospheric Chemistry and Physics, 15, 13 699–13 716, https://doi.org/10.5194/acp-15-13699-2015, 2015.

Vogel, B., Günther, G., Müller, R., Grooß, J.-U., Afchine, A., Bozem, H., Hoor, P., Krämer, M., Müller, S., Riese, M., Rolf, C., Spelten, N., Stiller, G. P., Ungermann, J., and Zahn, A.: Long-range transport pathways of tropospheric source gases originating in Asia into the northern lower stratosphere during the Asian monsoon season 2012, Atmospheric Chemistry and Physics, 16, 15 301–15 325, https://doi.org/10.5194/acp-16-15301-2016, 2016.

Vogel, B., Müller, R., Günther, G., Spang, R., Hanumanthu, S., Li, D., Riese, M., and Stiller, G. P.: Lagrangian simulations of the transport of young air masses to the top of the Asian monsoon anticyclone and into the tropical pipe, Atmospheric Chemistry and Physics, 19, 6007–6034, https://doi.org/10.5194/acp-19-6007-2019, 2019.

von Blohn, N., Diehl, K., Mitra, S. K., and Borrmann, S.: Wind tunnel experiments on the retention of trace gases during riming: nitric acid, hydrochloric acid, and hydrogen peroxide, Atmospheric Chemistry and Physics, 11, 11 569–11 579, https://doi.org/10.5194/acp-11-11569-2011, 2011.

von Blohn, N., Diehl, K., Nölscher, A., Jost, A., Mitra, S. K., and Borrmann, S.: The retention of ammonia and sulfur dioxide during riming of ice particles and dendritic snow flakes: laboratory experiments in the Mainz vertical wind tunnel, Journal of Atmospheric Chemistry, 70, 131–150, https://doi.org/10.1007/s10874-013-9261-x, 2013.

von Hobe, M., Grooß, J.-U., Günther, G., Konopka, P., Gensch, I., Krämer, M., Spelten, N., Afchine, A., Schiller, C., Ulanovsky, A., Sitnikov, N., Shur, G., Yushkov, V., Ravegnani, F., Cairo, F., Roiger, A., Voigt, C., Schlager, H., Weigel, R., Frey, W., Borrmann, S., Müller, R., and Stroh, F.: Evidence for heterogeneous chlorine activation in the tropical UTLS, Atmospheric Chemistry and Physics, 11, 241–256, https://doi.org/10.5194/acp-11-241-2011, 2011.

von Hobe, M., Ploeger, F., Konopka, P., Kloss, C., Ulanowski, A., Yushkov, V., Ravegnani, F., Volk, C. M., Pan, L. L., Honomichl, S. B., Tilmes, S., Kinnison, D. E., Garcia, R. R., and Wright, J. S.: Upward transport into and within the Asian monsoon anticyclone as inferred from StratoClim trace gas observations, Atmospheric Chemistry and Physics, 21, 1267–1285, https://doi.org/10.5194/acp-21-1267-2021, 2021.

Wagner, R., Bertozzi, B., Höpfner, M., Höhler, K., Möhler, O., Saathoff, H., and Leisner, T.: Solid Ammonium Nitrate Aerosols as Efficient Ice Nucleating Particles at Cirrus Temperatures, Journal of Geophysical Research: Atmospheres, 125, e2019JD032 248, https://doi.org/https://doi.org/10.1029/2019JD032248, e2019JD032248 2019JD032248, 2020.

Wang, M., Kong, W., Marten, R., He, X.-C., Chen, D., Pfeifer, J., Heitto, A., Kontkanen, J., Dada, L., Kürten, A., Yli-Juuti, T., Manninen, H. E., Amanatidis, S., Amorim, A., Baalbaki, R., Baccarini, A., Bell, D. M., Bertozzi, B., Bräkling, S., Brilke, S., Murillo, L. C., Chiu, R., Chu, B., Menezes, L.-P. D., Duplissy, J., Finkenzeller, H., Carracedo, L. G., Granzin, M., Guida, R., Hansel, A., Hofbauer, V., Krechmer, J., Lehtipalo, K., Lamkaddam, H., Lampimäki, M., Lee, C. P., Makhmutov, V., Marie, G., Mathot, S., Mauldin, R. L., Mentler, B., Müller, T., Onnela, A., Partoll, E., Petäjä, T., Philippov, M., Pospisilova, V., Ranjithkumar, A., Rissanen, M., Rörup, B., Scholz, W., Shen, J., Simon, M., Sipilä, M., Steiner, G., Stolzenburg, D., Tham, Y. J., Tomé, A., Wagner, A. C., Wang, D. S., Wang, Y., Weber, S. K., Winkler, P. M., Wlasits, P. J., Wu, Y., Xiao, M., Ye, Q., Zauner-Wieczorek, M., Zhou, X., Volkamer, R., Riipinen, I., Dommen, J., Curtius, J., Baltensperger, U., Kulmala, M., Worsnop, D. R., Kirkby, J., Seinfeld, J. H., El-Haddad, I., Flagan, R. C., and Donahue, N. M.: Rapid

growth of new atmospheric particles by nitric acid and ammonia condensation, Nature, 581, 184–189, https://doi.org/10.1038/s41586-020-2270-4, 2020.

Wang, M., Xiao, M., Bertozzi, B., Marie, G., Rörup, B., Schulze, B., Bardakov, R., He, X.-C., Shen, J., Scholz, W., Marten, R., Dada, L., Baalbaki, R., Lopez, B., Lamkaddam, H., Manninen, H. E., Amorim, A., Ataei, F., Bogert, P., Brasseur, Z., Caudillo, L., Menezes, L.-P. D., Duplissy, J., Ekman, A. M. L., Finkenzeller, H., Carracedo, L. G., Granzin, M., Guida, R., Heinritzi, M., Hofbauer, V., Höhler, K., Korhonen, K., Krechmer, J. E., Kürten, A., Lehtipalo, K., Mahfouz, N. G. A., Makhmutov, V., Massabò, D., Mathot, S., Mauldin, R. L., Mentler, B., Müller, T., Onnela, A., Petäjä, T., Philippov, M., Piedehierro, A. A., Pozzer, A., Ranjithkumar, A., Schervish, M., Schobesberger, S., Simon, M., Stozhkov, Y., Tomé, A., Umo, N. S., Vogel, F., Wagner, R., Wang, D. S., Weber, S. K., Welti, A., Wu, Y., Zauner-Wieczorek, M., Sipilä, M., Winkler, P. M., Hansel, A., Baltensperger, U., Kulmala, M., Flagan, R. C., Curtius, J., Riipinen, I., Gordon, H., Lelieveld, J., El-Haddad, I., Volkamer, R., Worsnop, D. R., Christoudias, T., Kirkby, J., Möhler, O., and Donahue, N. M.: Synergistic HNO_3–H_2SO_4–NH_3 upper tropospheric particle formation, Nature, 605, 483–489, https://doi.org/10.1038/s41586-022-04605-4, 2022.

Weigel, R., Hermann, M., Curtius, J., Voigt, C., Walter, S., Böttger, T., Lepukhov, B., Belyaev, G., and Borrmann, S.: Experimental characterization of the COndensation PArticle counting System for high altitude aircraft-borne application, Atmospheric Measurement Techniques, 2, 243–258, https://doi.org/10.5194/amt-2-243-2009, 2009.

Weigel, R., Borrmann, S., Kazil, J., Minikin, A., Stohl, A., Wilson, J. C., Reeves, J. M., Kunkel, D., de Reus, M., Frey, W., Lovejoy, E. R., Volk, C. M., Viciani, S., D'Amato, F., Schiller, C., Peter, T., Schlager, H., Cairo, F., Law, K. S., Shur, G. N., Belyaev, G. V., and Curtius, J.: In situ observations of new particle formation in the tropical upper troposphere: the role of clouds and the nucleation mechanism, Atmospheric Chemistry and Physics, 11, 9983–10 010, https://doi.org/10.5194/acp-11-9983-2011, 2011.

Weigel, R., Mahnke, C., Baumgartner, M., Dragoneas, A., Vogel, B., Ploeger, F., Viciani, S., D'Amato, F., Bucci, S., Legras, B., Luo, B., and Borrmann, S.: In situ observation of new particle formation (NPF) in the tropical tropopause layer of the 2017 Asian monsoon anticyclone – Part 1: Summary of StratoClim results, Atmospheric Chemistry and Physics, 21, 11 689–11 722, https://doi.org/10.5194/acp-21-11689-2021, 2021a.

Weigel, R., Mahnke, C., Baumgartner, M., Krämer, M., Spichtinger, P., Spelten, N., Afchine, A., Rolf, C., Viciani, S., D'Amato, F., Tost, H., and Borrmann, S.: In situ observation of new particle formation (NPF) in the tropical tropopause layer of the 2017 Asian monsoon anticyclone – Part 2: NPF inside ice clouds, Atmospheric Chemistry and Physics, 21, 13 455–13 481, https://doi.org/10.5194/acp-21-13455-2021, 2021b.

Wennberg, P. O.: Let's abandon the "high NOx" and "low NOx" terminology, IGAC News, 50, 3–4, 2013.

Williamson, C. J., Kupc, A., Axisa, D., Bilsback, K. R., Bui, T., Campuzano-Jost, P., Dollner, M., Froyd, K. D., Hodshire, A. L., Jimenez, J. L., Kodros, J. K., Luo, G., Murphy, D. M., Nault, B. A., Ray, E. A., Weinzierl, B., Wilson, J. C., Yu, F., Yu, P., Pierce, J. R., and Brock, C. A.: A large source of cloud condensation nuclei from new particle formation in the tropics, Nature, 574, 399–403, https://doi.org/10.1038/s41586-019-1638-9, 2019.

Xu, W., Croteau, P., Williams, L., Canagaratna, M., Onasch, T., Cross, E., Zhang, X., Robinson, W., Worsnop, D., and Jayne, J.: Laboratory characterization of an aerosol chemical speciation monitor with PM2.5 measurement capability, Aerosol Science and Technology, 51, 69–83, https://doi.org/10.1080/02786826.2016.1241859, 2017.

Yao, X., Rehbein, P. J., Lee, C. J., Evans, G. J., Corbin, J., and Jeong, C.-H.: A study on the extent of neutralization of sulphate aerosol through laboratory and field experiments using an ATOFMS and a GPIC, Atmos. Environ., 45, 6251 – 6256, https://doi.org/10.1016/j.atmosenv.2011.06.061, 2011.

Yu, P., Toon, O. B., Neely, R. R., Martinsson, B. G., and Brenninkmeijer, C. A. M.: Composition and physical properties of the Asian Tropopause Aerosol Layer and the North American Tropospheric Aerosol Layer, Geophysical Research Letters, 42, 2540–2546, https://doi.org/https://doi.org/10.1002/2015GL063181, 2015.

Yu, P., Rosenlof, K. H., Liu, S., Telg, H., Thornberry, T. D., Rollins, A. W., Portmann, R. W., Bai, Z., Ray, E. A., Duan, Y., Pan, L. L., Toon, O. B., Bian, J., and Gao, R.-S.: Efficient transport of tropospheric aerosol into the stratosphere via the Asian summer monsoon anticyclone, Proceedings of the National Academy of Sciences, 114, 6972–6977, https://doi.org/10.1073/pnas.1701170114, 2017.

Yuan, C., Lau, W. K. M., Li, Z., and Cribb, M.: Relationship between Asian monsoon strength and transport of surface aerosols to the Asian Tropopause Aerosol Layer (ATAL): interannual variability and decadal changes, Atmospheric Chemistry and Physics, 19, 1901–1913, https://doi.org/10.5194/acp-19-1901-2019, 2019.

Zhang, J., Wu, X., Liu, S., Bai, Z., Xia, X., Chen, B., Zong, X., and Bian, J.: In situ measurements and backward-trajectory analysis of high-concentration, fine-mode aerosols in the UTLS over the Tibetan Plateau, Environmental Research Letters, 14, 124 068, https://doi.org/10.1088/1748-9326/ab5a9f, 2019.

Zhang, Q., Wu, G., and Qian, Y.: The Bimodality of the 100 hPa South Asia High and its Relationship to the Climate Anomaly over East Asia in Summer, Journal of the Meteorological Society of Japan. Ser. II, 80, 733–744, https://doi.org/10.2151/jmsj.80.733, 2002.

Zhang, Q., Jimenez, J. L., Worsnop, D. R., and Canagaratna, M.: A Case Study of Urban Particle Acidity and Its Influence on Secondary Organic Aerosol, Environmental Science & Technology, 41, 3213–3219, https://doi.org/10.1021/es061812j, pMID: 17539528, 2007.

Zhou, W., Xu, W., Kim, H., Zhang, Q., Fu, P., Worsnop, D. R., and Sun, Y.: A review of aerosol chemistry in Asia: insights from aerosol mass spectrometer measurements, Environ. Sci.: Processes Impacts, 22, 1616–1653, https://doi.org/10.1039/D0EM00212G, 2020.

S1 Signal processing and data analysis for the ERICA-AMS

S1.1 Signal preparation and analysis

The ionized vapour is extracted by an extraction pulser working at a frequency of 50 kHz, resulting in a maximum m/z of above 700. The data acquisition card averages 20 000 extractions to one raw spectrum that is then transmitted to the computer and represents 0.4 s of measurement. One measurement cycle of the ERICA-AMS consists of 10 s or 25 raw spectra. 12 raw spectra (4.8 s) are taken while the shutter is open as representative for the aerosol measurement, whereas during 11 raw spectra (4.4 s) the shutter is closed for a background measurement (i.e. residual vacuum signal). Two raw spectra (0.8 s) are needed for the switching of the shutter and are discarded due to an undefined shutter position. One data file is recorded every five minutes. A sudden power interrupt prohibits the finalization of the data file, thus the last file of the flight is usually corrupted. In TofWare 2.5.7 we adjusted the settings to comply with the ERICA-AMS data. Executing *"setigoroption poundde-fine= tw_ACSM_diffSticks_dontNorm28"* and recompiling as well as activating the button *"Background is blocked beam (adv)"* prevents TofWare from normalization of each spectrum to m/z 28. This normalization is only practical in ACSM instruments, which the software was designed for. Due to our inhouse-built shutter unit, the software is unable to read the shutter position, thus we set it manually to $1-12$ (Total) and $14-24$ (Bkgnd), switch buf 13. The triggering of the shutter directly by the ADQ precludes potential shifts in the time scheme. We also insert the IE calibration factor (cf. section S1.2) and the sample flow rate into the instrument as measured with a Gilibrator (i.e. a value of 1.45 $\mathrm{cm^3 s^{-1}}$). In order to convert the raw spectra into an integrated unit mass resolution (UMR) spectrum, also called stick spectrum, an m/z calibration is needed to identify the signal peaks. We use a three-parameter fit of the form $p_1 \cdot m^{p_3} + p_2$ to the masses of CH^+ ($m/z = 13.0078$), O_2 (31.9898), SO_2 (63.9619), ^{182}W (181.948), ^{184}W (183.951) and ^{186}W (185.954). A time series of calibration values for each data point was used. TofWare calculates a time series of stick spectra according to the predefined values. The aerosol signal is represented by the "diff" spectrum, which is the difference of the measurement with an open shutter and a closed shutter. After excluding 16 data points as outliers and 1289 data points acquired during cloud passes (about 11.7 % of the data) the data basis for this publication is 9624 data points, 10 s each, resulting in a total of 26 h and 44 min of measurement time over all eight scientific flights.

S1.2 IE calibrations for StratoClim and fragmentation table

The conversion of the measured signal into a particle mass concentration is achieved by an ionization efficiency (IE) calibration implemented as the mass-based or bulk method (e.g. Drewnick et al., 2005). Therefore a polydisperse aerosol of a known substance (ammonium nitrate or ammonium sulfate) is generated by a nebulizer. A differential mobility analyzer (DMA) is used to select particles of a defined electromobility diameter. The particle number concentration measured by a condensation particle counter and the particle diameter are then used to calculate the total particulate mass concentration introduced into the instrument. By comparison with the acquired signal on the ERICA-AMS data acquisition card and the previously determined signal of single ions with the Software *"SingleIon2"* (TofWerk), the ionization efficiency of nitrate and the ionization efficiency relative to nitrate (RIE) of ammonium and sulfate is determined. Averaged over four calibrations, we found an IE calibration factor of 1965 $\mathrm{ions\,pg^{-1}}$, RIE(NH_4) = 4.37 and RIE(SO_4) = 0.97 to be valid for Flights 1 and 4-8. The calibration values for Flights 2 and 3 are based on one measurement with different settings and can be found in Table S1.

The attribution of the UMR signals to the chemical species of interest (e.g. nitrate, organic, ammonium, sulfate) is done by means of a so-called fragmentation table (Allan et al., 2004). Due to the large uncertainty of the mass peaks at m/z 16 and 29 concomitant with the relatively large air beam signal, the fragmentation table had to be modified for the ERICA-AMS. The ammonium signal at m/z 16 is not measured directly, but calculated out of the ammonium signal at m/z 17 using the fragmentation ratio $R_{16/17}$ determined during calibration (see Table S1). The organic signal at m/z 29 is assumed equal to the organic signal at m/z 43. This assumption is based on Fry et al. (2018), who introduced a correction to the nitrate signal for environments with high biogenic contribution to the organic mass concentration as well as low nitrate concentrations in their supplemental material. The correction can accordingly be based on the organic signal at m/z 29 or 43 using the same correction factor. Also the correct contribution of gaseous CO_2 to m/z 44 has to be considered, especially since the particulate organic signal at m/z 44 ($org44$) is crucial for the analysis of photo-oxidation state (see Section S1.6). Since small errors have

Table S1. IE calibrations relevant for the data set of this work

Date (YY-MM-DD)	calib. factor	RIE (NH_4)	RIE (SO_4)	$R_{16/17}$
17-06-29	1883	4.42	1.07	0.83
17-07-28	1956	4.36		0.79
17-09-08	2005	4.38	0.91	0.83
17-09-08	2014	4.31	0.93	0.83
avg	1965	4.37	0.97	0.82
calibration for flight 2 and 3				
17-07-28	1366	4.59	0.67	0.89

more severe consequences at low concentrations rather than at higher concentrations, we decided to adjust the level of $org44$ and organic to be zero at the highest potential temperatures above 460 K. While possibly leading to small errors at different conditions of instrument temperature and CO_2 levels, it is a good proxy for the quantification of small levels of organics found between 420 K and 440 K. We have also tried to estimate the CO_2 levels from filter measurements on the ground, which however lead to unreasonably low and even negative $org44$ and $organic$ levels in the stratosphere.

The collection efficiency of the vaporizer is depending on e.g. the chemical constituents of the aerosol particle. Middlebrook et al. (2012) developed a method to estimate the collection efficiency based on the measured chemical composition. We used this method to correct the acquired mass concentrations, since a high ammonium nitrate fraction as well as very acidic aerosol can be found in the ATAL and lower stratosphere, respectively. Both can lead to a significantly higher collection efficiency than the commonly assumed 0.5 (Allan et al., 2003a).

S1.3 Determination of the detection limit

To distinguish between aerosol signals and the noise level the lower detection limit of the ERICA-AMS has to be determined. While several methods are described in the literature, e.g. estimation from a reference measurement with particle free air through a HEPA filter (Allan et al., 2003b; Bahreini et al., 2003), from the background measurement (Drewnick et al., 2009) or the ion counting statistics (Allan et al., 2003b), these methods show significant downsides during airborne AMS operation. The determination of the noise during a filter measurement is only representative for a distinct time period of the flight, since vacuum background and temperature vary over time. The variation of the background measurement also cannot be used as a proxy for the noise, because most of the variation of the background signal is due to the vacuum which improved with flight time or varying temperatures rather than statistical noise.

We describe the background signal as

$$F(t) = T(t) + N(t) \tag{1}$$

where $T(t)$ denotes the trend due to improving vacuum or varying temperature and $N(t)$ describes the time dependent random noise, where the standard deviation over an arbitrary number of points n is given by

$$\sigma = \sqrt{\frac{\sum_n N(t)^2}{n}}. \tag{2}$$

The Savitzki-Golay filter (Savitzky and Golay, 1964) is a method for random noise reduction, and we used a third order smoothing over $m = 5$ data points resulting in a smoothed background signal

$$F_{smoothed}(t) = T(t) + N_{red}(t) \tag{3}$$

with reduced noise $N_{red}(t)$. The reduced noise shows a standard deviation of (Ziegler, 1981)

$$\sigma_{red} = \sqrt{\frac{\sum\limits_{n} N_{red}(t)^2}{n}} = \sqrt{\frac{3 \cdot (3m^2 - 7)}{4m \cdot (m^2 - 4)}} \cdot \sigma = \sqrt{\frac{17}{35}} \cdot \sigma. \tag{4}$$

Still, $T(t)$ and $N_{red}(t)$ remain unknown. However, we can calculate the difference function

$$D(t) = F(t) - F_{smoothed}(t) = N(t) - N_{red}(t) \tag{5}$$

which consists of noise functions with an expectation value of 0, each. The standard deviation σ of the original noise function $N(t)$ then represents the convolution of $\sigma_{red} = \sqrt{\frac{17}{35}} \cdot \sigma$ and $\sigma_D = \sqrt{\frac{\sum\limits_{n} D(t)^2}{n}}$, leading to the equation

$$\sigma^2 = \sigma_{red}^2 + \sigma_D^2 = \frac{35}{18} \cdot \sigma_D^2. \tag{6}$$

By calculating $\sigma_D = \sqrt{\frac{\sum\limits_{n} D(t)^2}{n}}$, we thus know the magnitude of the standard deviation $\sigma = \sqrt{\frac{35}{18}} \cdot \sigma_D$ of the background noise, despite of not being able to remove the noise.
The detection limit is then given by $3 \cdot \sigma$ in agreement with Allan et al. (2003b), Bahreini et al. (2003) and Drewnick et al. (2009). A similar method to determine the detection limit of a signal containing a trend has been introduced by Reitz (2011) and applied by Schulz et al. (2018). A comparison with detection limits calculated from the filter method based on lab measurements proves the validity of this method (Schulz, 2019; Hünig et al., 2021).

S1.4 Chloride signal in the ERICA-AMS during the Stratoclim 2017 aircraft campaign

During the StratoClim campaign we observed the chloride signal to be smaller than the detection limit even after averaging over up to two hours of flight time at the same altitude level. Detectable amounts of particulate chloride were only found inside the boundary layer, which is not subject of this publication. Chloride has been excluded from the analysis of this study, including total mass, mass fraction, acidity balance.

S1.5 Temperature dependence of the ERICA-AMS signal

The signal of the air beam strongly varied during each flight by up to 40 %. We found the signal to increase with decreasing temperature inside the pressurized barrel. Lab experiments with a selective heating of different components showed a dependence of the signal with the temperature of the MCP, whereas heating or cooling of other instrument components (sample air inlet, signal amplifiers, HV generator, data acquisition card) showed much less influence on the detected signal. We conclude that the variation of the air beam signal is caused by the temperature dependence of the MCP gain as was previously examined by Siddiqui (1979) and Slater and Timothy (1993). The signal dependence on temperature affects the aerosol signal the same way as the air beam. We therefore corrected all data according to this variation, commonly known as air beam correction (Allan et al., 2003b).

S1.6 Analysis of the oxidation state of organics

Among the common species - organics, nitrate, ammonium, sulfate, and chloride - the fragmentation table can also be used to generate signals of species at a specific m/z. For example, $org43$ and $org44$ are the contributions of m/z 43 and 44, respectively, to the total organic signal (denoted as "organics"). The relative contribution to the organic signal is $f_{43} = \frac{org43}{organics}$ and $f_{44} = \frac{org44}{organics}$. Ng et al. (2010) showed, that these fractions indicate the oxidative ageing of organic aerosols. A high value of f_{43} (resulting mainly from $C_2H_3O^+$ ions) indicate fresh organics, while oxidative ageing leads to an increasing contribution

of organic acids, which results in a higher value of f_{44} (mainly CO_2^+ ions). The values for f_{44} are plotted against f_{43} for each data point of the StratoClim campaign (Fig. 11 in the main paper). We averaged the data over 90 s and only displayed values where the total organic signal as well as the organic signals at m/z 43 and 44 are above the detection limit. The median values and interquartiles for different ranges of potential temperature are indicated by black rectangular boxes. Here all those data points were considered as valid, where the total organics signal was above the detection limit. The lines of the black triangle indicate the region, where the majority of ambient organic aerosol can be found (Ng et al., 2010). Data points in the lower part of the triangle indicate fresh and primary aerosol (Ng et al., 2011). The closer the data point tend to the upper left corner, the higher is the photooxidative ageing of the aerosol.

An additional measure for the photooxidative state can be expressed by the fraction $R_{44/43} = \frac{f_{44}}{f_{43}}$. Here, higher photooxidative states result in a higher value of $R_{44/43}$. $R_{44/43}$ is displayed against altitude and θ in Fig. 14 in the main paper.

S2 Signal processing and data analysis for the ERICA-LAMS

S2.1 Particle classification

The ERICA-LAMS bipolar spectra of single particles are recorded in four channels (two channels of different full scale range for each polarity). The recorded spectra in the four channels are combined into two spectra, one for each polarity. In total, 109,453 particles were chemically analyzed by the ERICA-LAMS during the StratoClim research flights when sampling outside clouds. Of all collected spectra 92 % were dual polarity, and 99 % include particle size information. We applied the separation between measurements inside and outside clouds, since the aerosol inlet was not suited to conduct measurements inside clouds. CDP data were used to separate between the two events, as explained in Sect. 2.

We used the CRISP software package (Concise Retrieval of Information from Single Particles; Klimach, 2012) to perform m/z calibration of mass spectra and peak area integration. The CRISP software package was further used to classify the spectra into different particle types. For particle classification, we combined two commonly used methods: the fuzzy c-means clustering (e.g. Hinz et al., 1999; Roth et al., 2016; Schneider et al., 2021) and the marker ion method (Köllner et al., 2017, 2021). The applied clustering and markering conditions and parameters are summarized in Tables S2 and S3.

In a first step, we applied fuzzy c-means clustering (Clustering 1, see Table S2) according to Schneider et al. (2021) to identify particles containing meteoric material. With the remaining spectra, we repeated fuzzy c-means clustering (Clustering 2, 3, 4, see Table S2) to identify elemental carbon (EC) particles. In a next step, the marker ion method was used to classify the remaining spectra. We examined, if one of the following marker species was included in the single particle spectra, which means, if the respective ion markers were above the ion peak area threshold: K, Si, P, Na, Mg, V, Fe, Ca, Cr, Ti, Cu, Li, Pb, Hg, and Zn (Table S3). The ion peak area threshold for the ERICA-LAMS data during StratoClim 2017 is 7 $\mathrm{mV} \cdot \mathrm{sample}$ for both polarities (Hünig et al., 2021). 1 sample of the data acquisition card corresponds to 1.6 ns. So far, our aim was to identify particles including primary components, i.e. meteoric material, EC, anthropogenic metals, and minerals. As a result, we summed up all particles containing primary components, providing the so-called Primary or Mixed ~~particle~~ Type.

In a final step, we analysed the remaining particles for particle spectra with dominant ion markers at m/z +12, +24, +36, +48 (C_{1-4}^+), and +39 (K^+) (the so-called Low EC/OC particle type) in the StratoClim 2017 data set. We found 5235 particles of this type (out of 109 453). However, it is not clear if this particle type implies the presence of (aged) EC and/or organic carbon (OC) (e.g. Moffet and Prather, 2009; Healy et al., 2009; Zanatta et al., 2019), both mixed with potassium. Hence, the origin of low EC/OC needs further investigation. For this reason, we classified this particle type as "Unidentified" and excluded this particle type from the further analysis.

Besides the Primary/Mixed and the Unidentified ~~particle~~ Type, we obtained a particle type that consists of all remaining spectra and is characterized by the sole presence of secondary components in single particle spectra (the so-called Secondary ~~particle~~ Type). We further sorted the Secondary Type into Type 1, showing a dominant peak at m/z 30, and Type 2, showing other peaks to be larger than m/z 30. ~~We further sub-divided the secondary particle type in a type 1 with dominant m/z 30 peak and a class with non-dominant m/z 30 peak.~~ For the latter class, other components like ammonium and C_n-structure are dominant.

Table S2. Particle classification by fuzzy c-means clustering. Parameters for the different clustering steps used for the analysis are given. The respective particle types and numbers are shown.

Step	Ion type	Preprocessing	Normalization	Distance metric	Initialization Startcluster Number/Difference	Fuzzifier/ Fuzzy abort	Particle type / number characterized by...
Clustering 1[1] of 102,009 dual-polarity spectra	Cation	power each m/z by 0.5	Sum	Correlation	20 / 0.9	1.3/1e-5	1) Meteoric particle / 18467 Dominant m/z +24/25/26 (Mg^+) and +54/56 (Fe^+) 2) Dominant Na^+,K^+,Fe^+ / 934
Clustering 2[2] of 82,608 dual-polarity spectra	Anion+ Cation	power each m/z by 0.5	Sum	Correlation	20 / 0.7	1.3/1e-5	3) Elemental Carbon (EC) / 2534 m/z +12,+24,...,+132 (C^+_{1-11}) and m/z -24,-36...,-108 (C^-_{2-9})
Clustering 3[2] of 80,074 dual-polarity spectra	Anion+ Cation	power each m/z by 0.5	Sum	Correlation	40 / 0.7	1.3/1e-5	3) Elemental Carbon (EC) / 90 m/z +12,+24,...,+84 (C^+_{1-7}) and m/z -24,-36...,-72 (C^-_{2-6})
Clustering 4[2] of 108 single anion spectra	Anion	power each m/z by 0.5	Sum	Correlation	5 / 0.7	1.3/1e-5	3) Elemental Carbon (EC) / 9 m/z -24,-36...,-132 (C^-_{2-11})

Given reference numbers are defined as follows: [(1)]Schneider et al. (2021),[(2)]Roth (2014).

Table S3. Particle classification by marker species and associated ion markers applied in this study.

Marker species	Ion markers
Potassium (K)	m/z +39/41 (K^+)
Silicon (Si)	m/z +28 (Si^+) and m/z -60 (SiO_2^-) and -76 (SiO_3^-)
Phosphorus (P)	m/z -63 (PO_2^-) and -79 (PO_3^+)
Sodium (Na)	m/z +23 (Na^+)
Magnesium (Mg)	m/z +24/25/26 (Mg^+)
Vanadium (V)	m/z +51 (V^+) and +67 (VO^+)
Iron (Fe)	m/z +54/56 (Fe^+)
Calcium (Ca)	m/z +40 (Ca^+)
Chromium (Cr)	m/z +52/53 (Cr^+) and +68 (CrO^+) and +84 (CrO_2^+)
Titanium (Ti)	m/z +48 (Ti^+) and +64 (TiO^+)
Copper (Cu)	m/z +63/65 (Cu^+)
Lithium (Li)	m/z +7 (Li^+)
Lead (Pb)	m/z +206/207/208 (Pb^+)
Mercury (Hg)	m/z +199/200/202 (Hg^+)
Zinc (Zn)	m/z +64/66/68 (Zn^+)
Low elemental or organic carbon (Low EC/OC)	dominant m/z +12,+24,+36,+48 (C_{1-4}^+) and dominant m/z +39 (K^+)

S2.2 Uncertainty analysis

ERICA-LAMS particle number concentration at the first detection stage (N_0)

The absolute uncertainty of the averaged ERICA-LAMS particle number concentration at the first detection stage for each bin ($\sigma_{N_0}^{\text{abs}}$) is calculated based on Poisson statistics:

$$\sigma_{N_0}^{\text{abs}} = N_0 \cdot \sigma_{N_0}^{\text{rel}}, \tag{7}$$

with the $\sigma_{N_0}^{\text{rel}}$ that is defined as follows:

$$\sigma_{N_0}^{\text{rel}} = \frac{1}{\sqrt{C_0}}, \tag{8}$$

with the averaged ERICA-LAMS particle counts at the first detection stage for each bin (C_0).

ERICA-LAMS particle fraction (PF)

The absolute uncertainty of the ERICA-LAMS particle fraction for each bin (σ_{PF}^{abs}) is calculated using binomial statistics:

$$\sigma_{PF}^{\text{abs}} = \frac{\sqrt{N_{\text{hits}} \cdot PF \cdot (1 - PF)}}{N_{\text{hits}}}, \tag{9}$$

with the number of particles that are successfully ionized by the desorption laser and create a mass spectrum (N_{hits}) and the PF.

ERICA-LAMS scaled number concentration ($PF{\cdot}N_0$)

The absolute uncertainty of the ERICA-LAMS scaled number concentration for each bin ($\sigma_{PF\cdot N_0}^{\text{abs}}$) is calculated using Gaussian propagation of uncertainties:

$$\sigma_{PF\cdot N_0}^{\text{abs}} = \sqrt{\left(PF \cdot \sigma_{N_0}^{\text{abs}}\right)^2 + \left(N_0 \cdot \sigma_{PF}^{\text{abs}}\right)^2}. \tag{10}$$

S3 Additional figures

An overview of the measurement time in each altitude range is provided in Fig. S1.
In Fig. S2 the mass concentration profiles of organics and nitrate are compared. A Gaussian fit shows, that the profile of organic has its mode about 5 K higher and is about 10 K broader ($1/\sqrt{e}$ full width) compared the the nitrate profile of the ATAL.

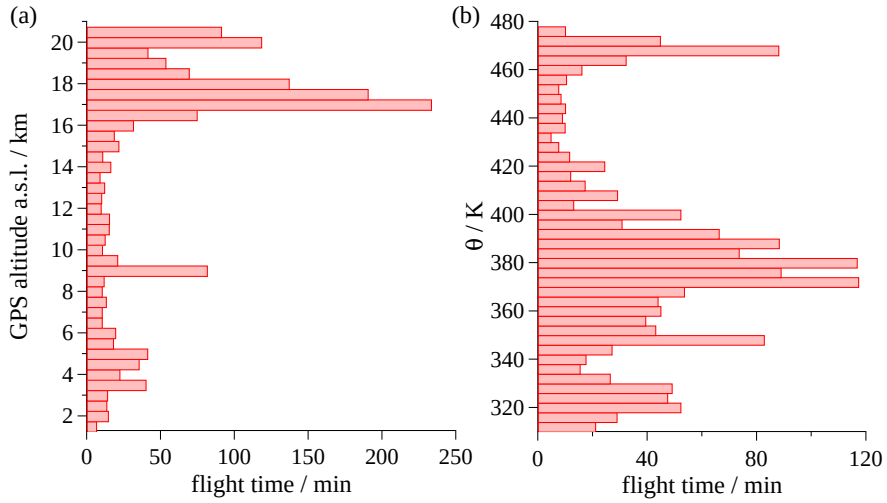

Figure S1. Vertical distribution of the accumulated measurement times of the ERICA-AMS in each (a) altitude and (b) θ bin during the whole StratoClim 2017 field deployment.

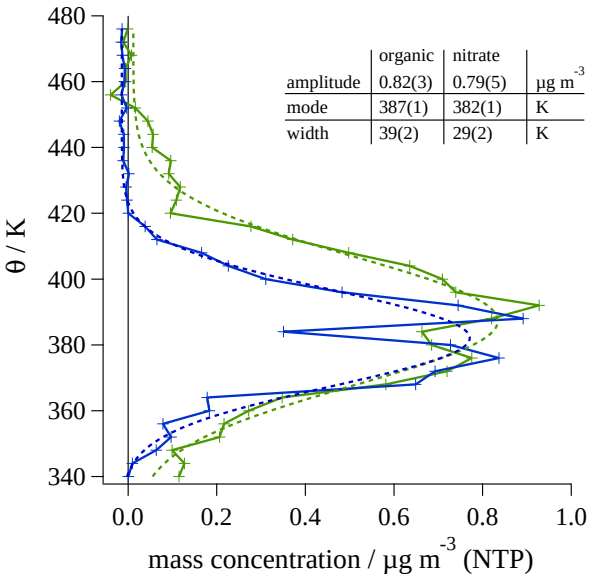

Figure S2. Gaussian fit to the vertical distribution of nitrate and organic mass concentrations, showing the lower edge is similar, but organics reach higher. The width parameter represents the $1/\sqrt{e}$ full width (2σ).

S3.1 Profiles of each flight

The vertical profile measured during each measurement flight is displayed in Fig. S3 to Fig. S10 against GPS altitude and potential temperature θ as reference for further studies.

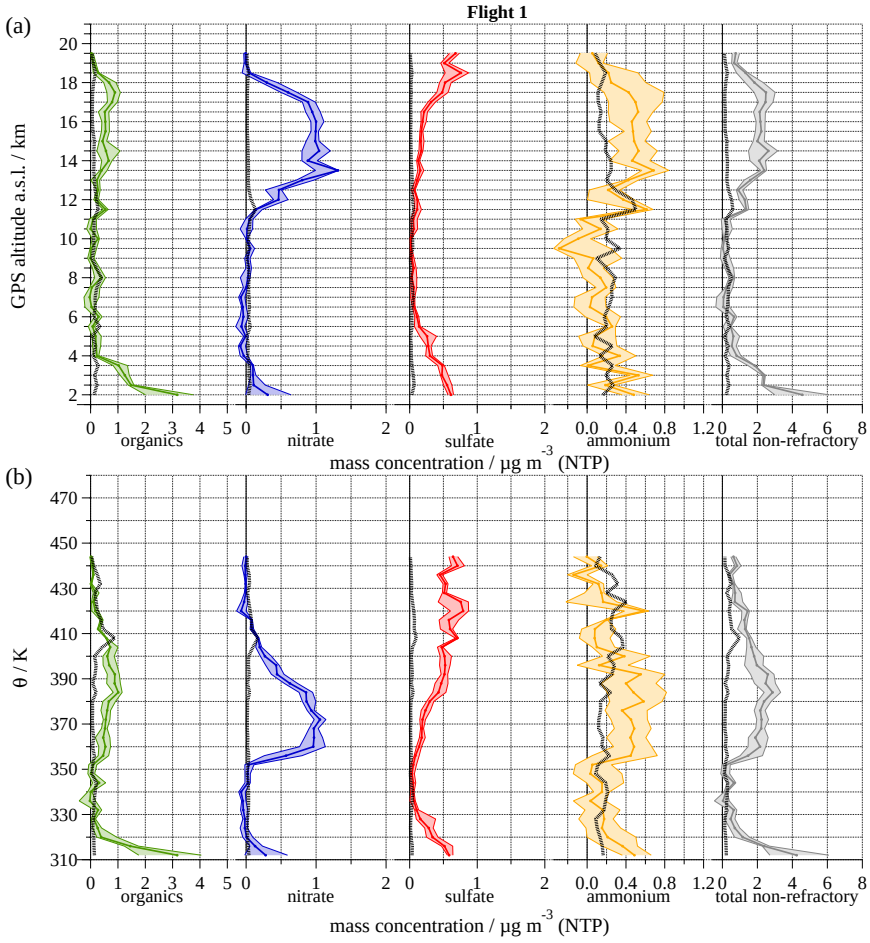

Figure S3. ERICA-AMS mass concentrations of particulate organics (green), nitrate (blue), sulfate (red), and ammonium (NH_4, orange) as a function of (a) GPS altitude and (b) potential temperature θ measured during research Flight 1 on 27 July. The thick line and the shaded area represent the median and $25th/75th$ percentiles in the corresponding altitude or θ bin. The right panel displays the sum of all species measured by the ERICA-AMS (grey). For each altitude bin the detection limit is displayed as a dotted line.

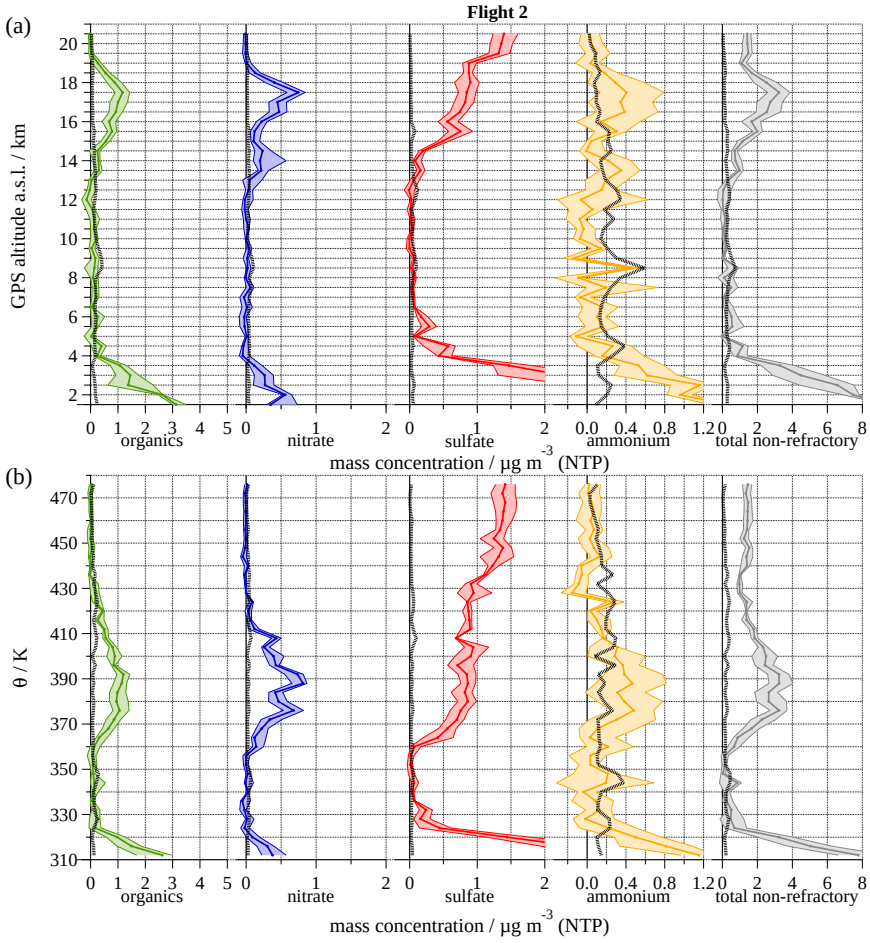

Figure S4. ERICA-AMS mass concentrations of particulate organics (green), nitrate (blue), sulfate (red), and ammonium (NH_4, orange) as a function of (a) GPS altitude and (b) potential temperature θ measured during research Flight 2 on 29 July. The thick line and the shaded area represent the median and $25th/75th$ percentiles in the corresponding altitude or θ bin. The right panel displays the sum of all species measured by the ERICA-AMS (grey). For each altitude bin the detection limit is displayed as a dotted line.

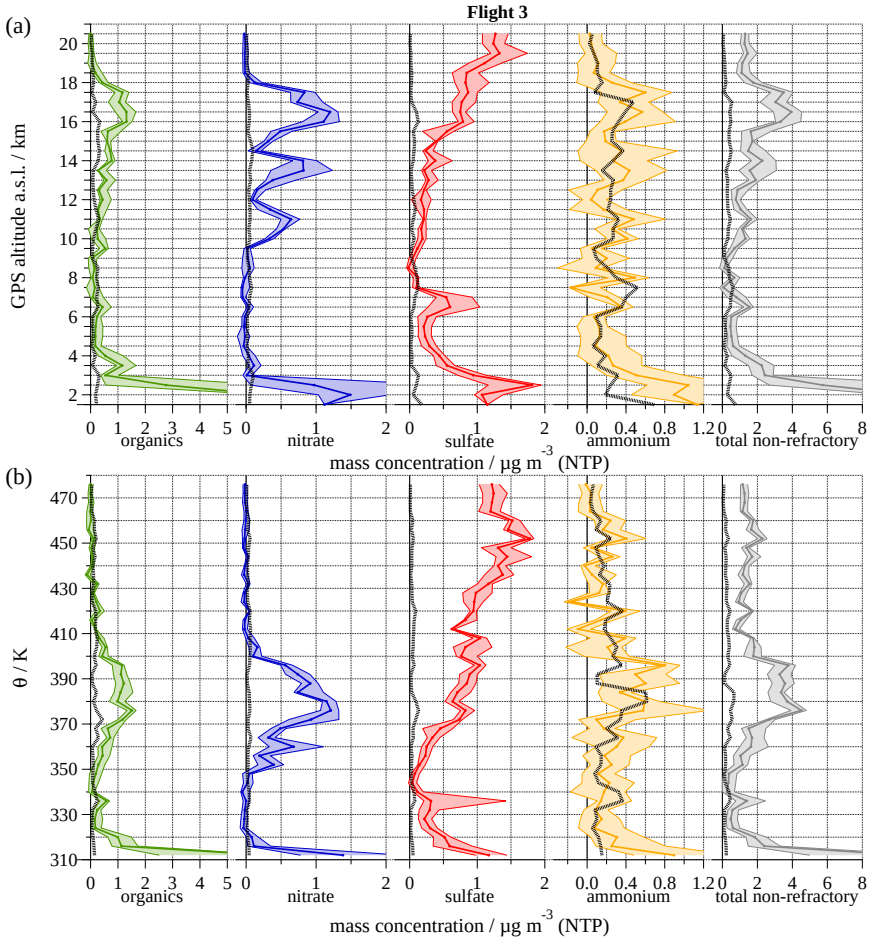

Figure S5. ERICA-AMS mass concentrations of particulate organics (green), nitrate (blue), sulfate (red), and ammonium (NH_4, orange) as a function of (a) GPS altitude and (b) potential temperature θ measured during research Flight 3 on 31 July. The thick line and the shaded area represent the median and $25th/75th$ percentiles in the corresponding altitude or θ bin. The right panel displays the sum of all species measured by the ERICA-AMS (grey). For each altitude bin the detection limit is displayed as a dotted line.

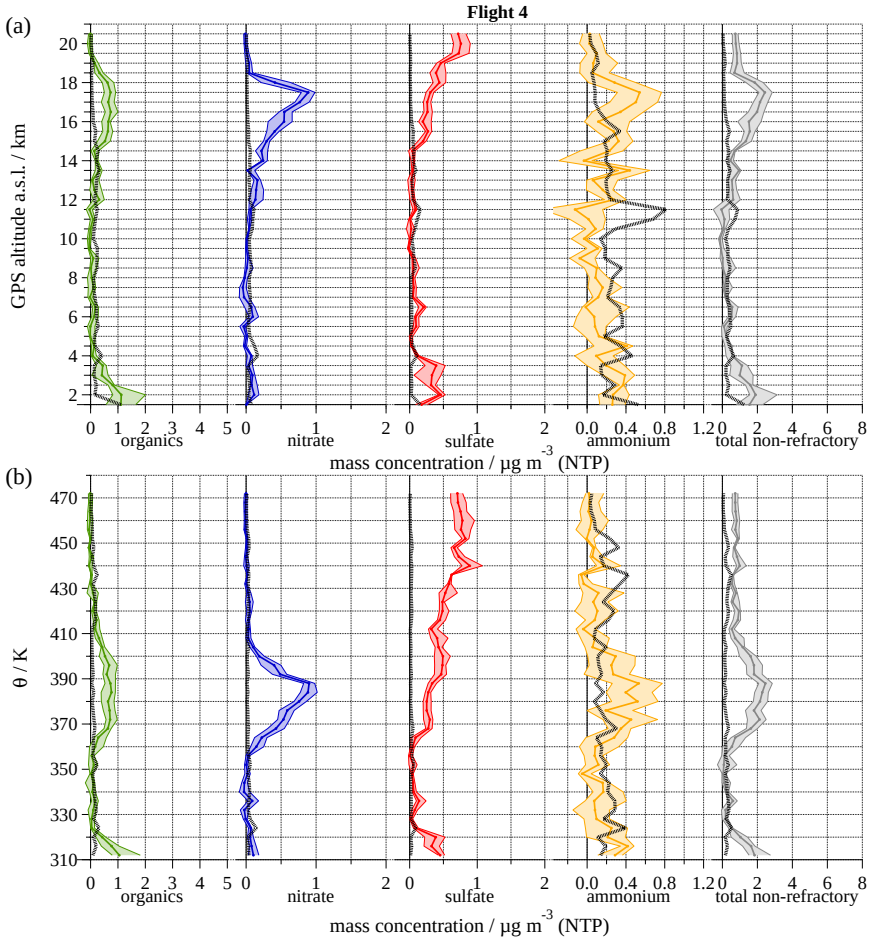

Figure S6. ERICA-AMS mass concentrations of particulate organics (green), nitrate (blue), sulfate (red), and ammonium (NH_4, orange) as a function of (a) GPS altitude and (b) potential temperature θ measured during research Flight 4 on 2 August. The thick line and the shaded area represent the median and $25th/75th$ percentiles in the corresponding altitude or θ bin. The right panel displays the sum of all species measured by the ERICA-AMS (grey). For each altitude bin the detection limit is displayed as a dotted line.

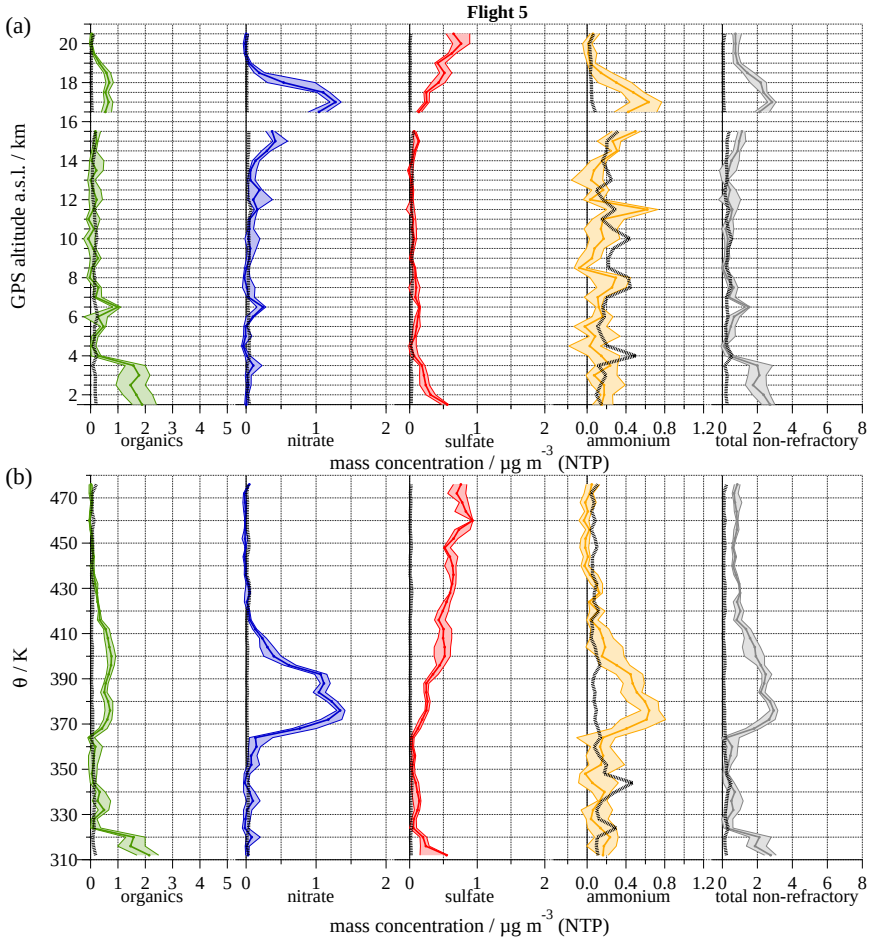

Figure S7. ERICA-AMS mass concentrations of particulate organics (green), nitrate (blue), sulfate (red), and ammonium (NH_4, orange) as a function of (a) GPS altitude and (b) potential temperature θ measured during research Flight 5 on 4 August. The thick line and the shaded area represent the median and $25th/75th$ percentiles in the corresponding altitude or θ bin. The right panel displays the sum of all species measured by the ERICA-AMS (grey). For each altitude bin the detection limit is displayed as a dotted line.

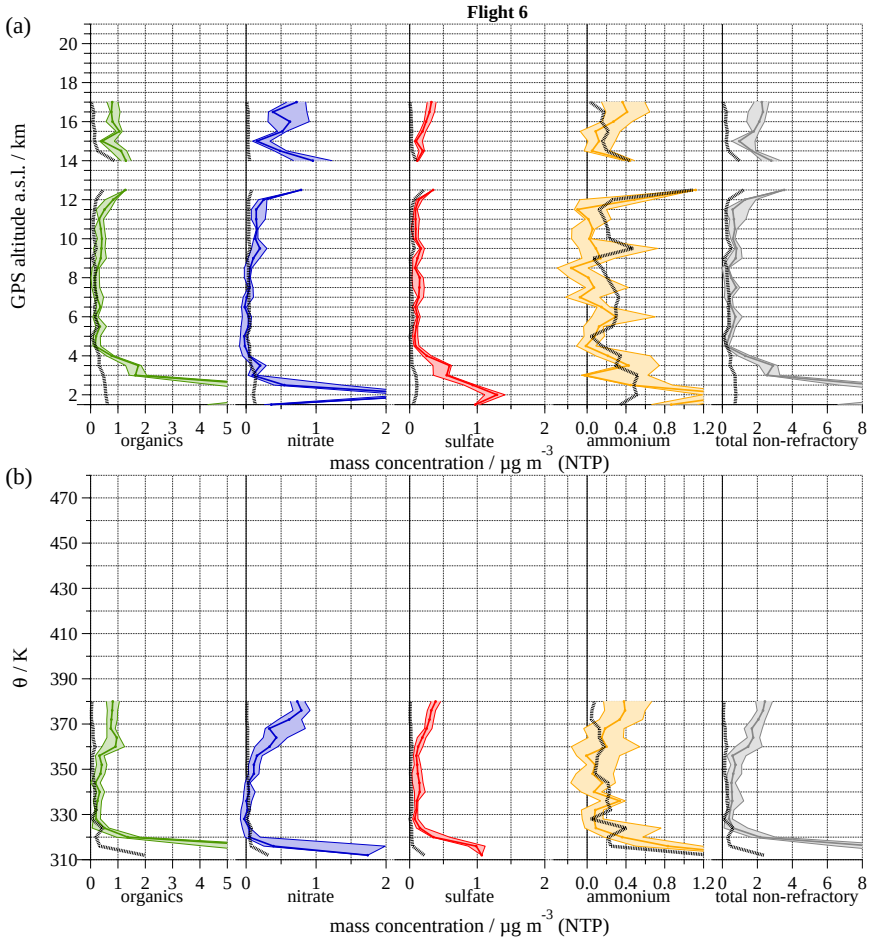

Figure S8. ERICA-AMS mass concentrations of particulate organics (green), nitrate (blue), sulfate (red), and ammonium (NH_4, orange) as a function of (a) GPS altitude and (b) potential temperature θ measured during research Flight 6 on 6 August. The thick line and the shaded area represent the median and $25th/75th$ percentiles in the corresponding altitude or θ bin. The right panel displays the sum of all species measured by the ERICA-AMS (grey). For each altitude bin the detection limit is displayed as a dotted line.

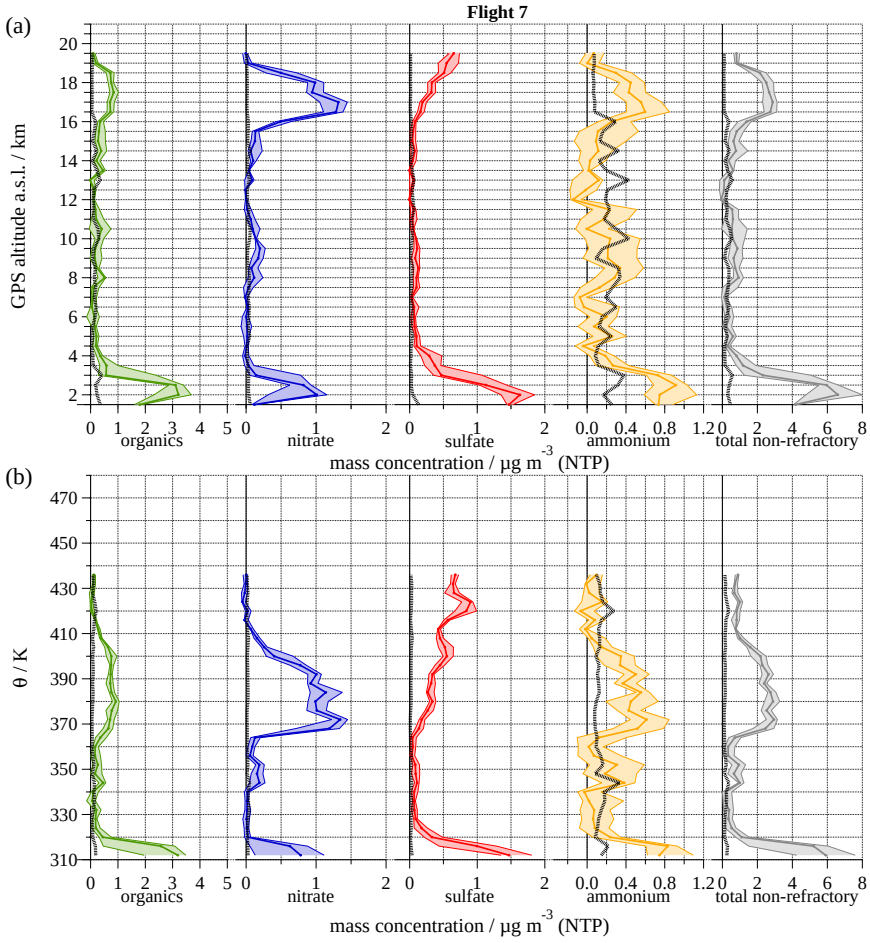

Figure S9. ERICA-AMS mass concentrations of particulate organics (green), nitrate (blue), sulfate (red), and ammonium (NH_4, orange) as a function of (a) GPS altitude and (b) potential temperature θ measured during research Flight 7 on 8 August. The thick line and the shaded area represent the median and $25th/75th$ percentiles in the corresponding altitude or θ bin. The right panel displays the sum of all species measured by the ERICA-AMS (grey). For each altitude bin the detection limit is displayed as a dotted line.

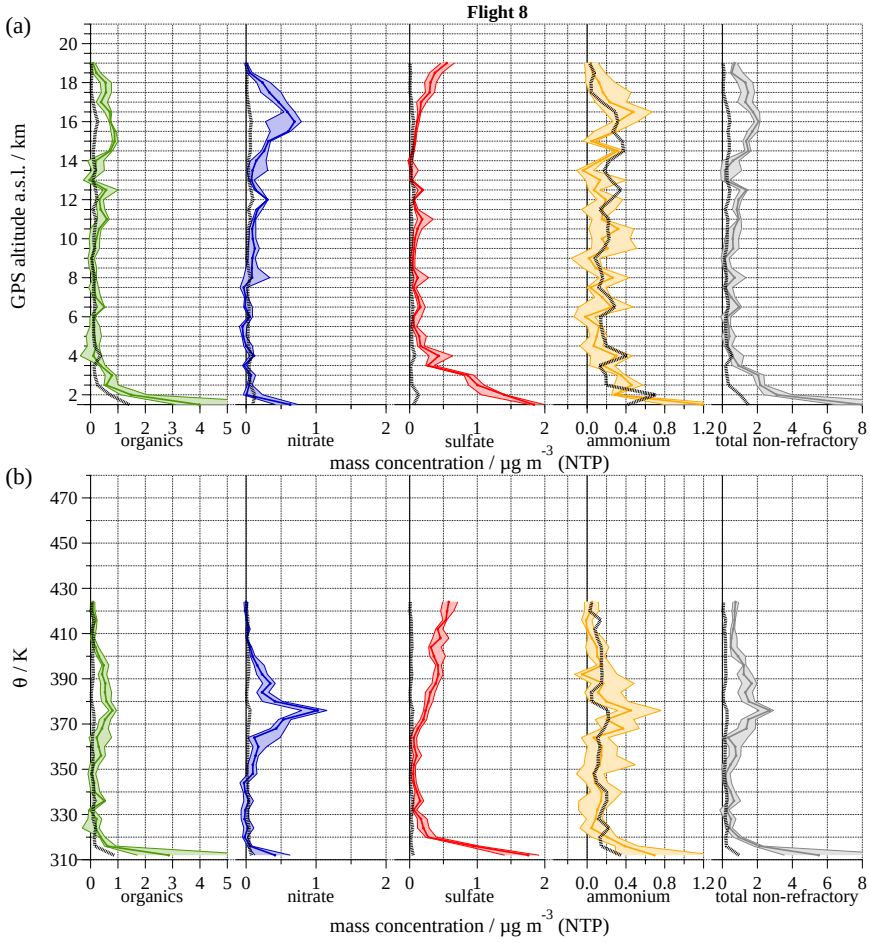

Figure S10. ERICA-AMS mass concentrations of particulate organics (green), nitrate (blue), sulfate (red), and ammonium (NH_4, orange) as a function of (a) GPS altitude and (b) potential temperature θ measured during research Flight 8 on 10 August. The thick line and the shaded area represent the median and $25th/75th$ percentiles in the corresponding altitude or θ bin. The right panel displays the sum of all species measured by the ERICA-AMS (grey). For each altitude bin the detection limit is displayed as a dotted line.

References

Allan, J. D., Alfarra, M. R., Bower, K. N., Williams, P. I., Gallagher, M. W., Jimenez, J. L., McDonald, A. G., Nemitz, E., Canagaratna, M. R., Jayne, J. T., Coe, H., and Worsnop, D. R.: Quantitative sampling using an Aerodyne aerosol mass spectrometer 2. Measurements of fine particulate chemical composition in two U.K. cities, Journal of Geophysical Research: Atmospheres, 108, https://doi.org/https://doi.org/10.1029/2002JD002359, https://agupubs.onlinelibrary.wiley.com/doi/abs/10.1029/2002JD002359, 2003a.

Allan, J. D., Jimenez, J. L., Williams, P. I., Alfarra, M. R., Bower, K. N., Jayne, J. T., Coe, H., and Worsnop, D. R.: Quantitative sampling using an Aerodyne aerosol mass spectrometer 1. Techniques of data interpretation and error analysis, Journal of Geophysical Research: Atmospheres, 108, https://doi.org/https://doi.org/10.1029/2002JD002358, https://agupubs.onlinelibrary.wiley.com/doi/abs/10.1029/2002JD002358, 2003b.

Allan, J. D., Delia, A. E., Coe, H., Bower, K. N., Alfarra, M., Jimenez, J. L., Middlebrook, A. M., Drewnick, F., Onasch, T. B., Canagaratna, M. R., Jayne, J. T., and Worsnop, D. R.: A generalised method for the extraction of chemically resolved mass spectra from Aerodyne aerosol mass spectrometer data, Journal of Aerosol Science, 35, 909–922, https://doi.org/10.1016/j.jaerosci.2004.02.007, https://www.sciencedirect.com/science/article/pii/S0021850204000229, 2004.

Bahreini, R., Jimenez, J. L., Wang, J., Flagan, R. C., Seinfeld, J. H., Jayne, J. T., and Worsnop, D. R.: Aircraft-based aerosol size and composition measurements during ACE-Asia using an Aerodyne aerosol mass spectrometer, Journal of Geophysical Research: Atmospheres, 108, https://doi.org/https://doi.org/10.1029/2002JD003226, https://agupubs.onlinelibrary.wiley.com/doi/abs/10.1029/2002JD003226, 2003.

Drewnick, F., Hings, S. S., DeCarlo, P., Jayne, J. T., Gonin, M., Fuhrer, K., Weimer, S., Jimenez, J. L., Demerjian, K. L., Borrmann, S., and Worsnop, D. R.: A New Time-of-Flight Aerosol Mass Spectrometer (TOF-AMS)—Instrument Description and First Field Deployment, Aerosol Science and Technology, 39, 637–658, https://doi.org/10.1080/02786820500182040, https://doi.org/10.1080/02786820500182040, 2005.

Drewnick, F., Hings, S. S., Alfarra, M. R., Prevot, A. S. H., and Borrmann, S.: Aerosol quantification with the Aerodyne Aerosol Mass Spectrometer: detection limits and ionizer background effects, Atmospheric Measurement Techniques, 2, 33–46, https://doi.org/10.5194/amt-2-33-2009, https://amt.copernicus.org/articles/2/33/2009/, 2009.

Fry, J. L., Brown, S. S., Middlebrook, A. M., Edwards, P. M., Campuzano-Jost, P., Day, D. A., Jimenez, J. L., Allen, H. M., Ryerson, T. B., Pollack, I., Graus, M., Warneke, C., de Gouw, J. A., Brock, C. A., Gilman, J., Lerner, B. M., Dubé, W. P., Liao, J., and Welti, A.: Secondary organic aerosol (SOA) yields from NO_3 radical + isoprene based on nighttime aircraft power plant plume transects, Atmospheric Chemistry and Physics, 18, 11 663–11 682, https://doi.org/10.5194/acp-18-11663-2018, https://acp.copernicus.org/articles/18/11663/2018/, 2018.

Healy, R. M., O'Connor, I. P., Hellebust, S., Allanic, A., Sodeau, J. R., and Wenger, J. C.: Characterisation of single particles from in-port ship emissions, Atmospheric Environment, 43, 6408–6414, https://doi.org/https://doi.org/10.1016/j.atmosenv.2009.07.039, https://www.sciencedirect.com/science/article/pii/S1352231009006529, 2009.

Hinz, K. P., Greweling, M., Drews, F., and Spengler, B.: Data processing in on-line laser mass spectrometry of inorganic, organic, or biological airborne particles, J. Am. Soc. Mass Spectrom., 10, 648–660, https://doi.org/10.1016/S1044-0305(99)00028-8, 1999.

Hünig, A., Appel, O., Dragoneas, A., Molleker, S., Clemen, H.-C., Helleis, F., Klimach, T., Köllner, F., Böttger, T., Drewnick, F., Schneider, J., and Borrmann, S.: Design, characterization, and first field deployment of a novel aircraft-based aerosol mass spectrometer combining the laser ablation and flash vaporization techniques, Atmospheric Measurement Techniques Discussions, 2021, 1–43, https://doi.org/10.5194/amt-2021-271, https://amt.copernicus.org/preprints/amt-2021-271/, 2021.

Klimach, T.: Chemische Zusammensetzung der Aerosole: Design und Datenauswertung eines Einzelpartikel-Laserablationsmassenspektrometers, Ph.D. thesis, Johannes-Gutenberg Universität Mainz, 2012.

Köllner, F., Schneider, J., Willis, M. D., Klimach, T., Helleis, F., Bozem, H., Kunkel, D., Hoor, P., Burkart, J., Leaitch, W. R., Aliabadi, A. A., Abbatt, J. P. D., Herber, A. B., and Borrmann, S.: Particulate trimethylamine in the summertime Canadian high Arctic lower troposphere, Atmos. Chem. Phys., 17, 13 747–13 766, https://doi.org/10.5194/acp-17-13747-2017, 2017.

Köllner, F., Schneider, J., Willis, M. D., Schulz, H., Kunkel, D., Bozem, H., Hoor, P., Klimach, T., Helleis, F., Burkart, J., Leaitch, W. R., Aliabadi, A. A., Abbatt, J. P. D., Herber, A. B., and Borrmann, S.: Chemical composition and source attribution of sub-micrometre aerosol particles in the summertime Arctic lower troposphere, Atmospheric Chemistry and Physics, 21, 6509–6539, https://doi.org/10.5194/acp-21-6509-2021, https://acp.copernicus.org/articles/21/6509/2021/, 2021.

Middlebrook, A. M., Bahreini, R., Jimenez, J. L., and Canagaratna, M. R.: Evaluation of Composition-Dependent Collection Efficiencies for the Aerodyne Aerosol Mass Spectrometer using Field Data, Aerosol Science and Technology, 46, 258–271, https://doi.org/10.1080/02786826.2011.620041, https://doi.org/10.1080/02786826.2011.620041, 2012.

Moffet, R. C. and Prather, K. A.: In-situ measurements of the mixing state and optical properties of soot with implications for radiative forcing estimates, P. Natl. Acad. Sci., 106, 11 872–11 877, https://doi.org/10.1073/pnas.0900040106, 2009.

Ng, N. L., Canagaratna, M. R., Zhang, Q., Jimenez, J. L., Tian, J., Ulbrich, I. M., Kroll, J. H., Docherty, K. S., Chhabra, P. S., Bahreini, R., Murphy, S. M., Seinfeld, J. H., Hildebrandt, L., Donahue, N. M., DeCarlo, P. F., Lanz, V. A., Prévôt, A. S. H., Dinar, E., Rudich, Y., and Worsnop, D. R.: Organic aerosol components observed in Northern Hemispheric datasets from Aerosol Mass Spectrometry, Atmospheric Chemistry and Physics, 10, 4625–4641, https://doi.org/10.5194/acp-10-4625-2010, https://acp.copernicus.org/articles/10/4625/2010/, 2010.

Ng, N. L., Canagaratna, M. R., Jimenez, J. L., Chhabra, P. S., Seinfeld, J. H., and Worsnop, D. R.: Changes in organic aerosol composition with aging inferred from aerosol mass spectra, Atmos. Chem. Phys., 11, 6465–6474, https://doi.org/10.5194/acp-11-6465-2011, 2011.

Reitz, P.: Chemical composition measurements of cloud condensation nuclei and ice nuclei by aerosol mass spectrometry, Ph.D. thesis, Johannes Gutenberg-Universität Mainz, 2011.

Roth, A.: Untersuchungen von Aerosolpartikeln und Wolkenresidualpartikeln mittels Einzelpartikel-Massenspektrometrie und optischen Methoden, Ph.D. thesis, Johannes Gutenberg-Universität Mainz, 2014.

Roth, A., Schneider, J., Klimach, T., Mertes, S., van Pinxteren, D., Herrmann, H., and Borrmann, S.: Aerosol properties, source identification, and cloud processing in orographic clouds measured by single particle mass spectrometry on a central European mountain site during HCCT-2010, Atmos. Chem. Phys., 16, 505–524, https://doi.org/10.5194/acp-16-505-2016, 2016.

Savitzky, A. and Golay, M. J. E.: Smoothing and Differentiation of Data by Simplified Least Squares Procedures, Analytical Chemistry, 36, 1627–1639, https://doi.org/10.1021/ac60214a047, https://doi.org/10.1021/ac60214a047, 1964.

Schneider, J., Weigel, R., Klimach, T., Dragoneas, A., Appel, O., Hünig, A., Molleker, S., Köllner, F., Clemen, H.-C., Eppers, O., Hoppe, P., Hoor, P., Mahnke, C., Krämer, M., Rolf, C., Grooß, J.-U., Zahn, A., Obersteiner, F., Ravegnani, F., Ulanovsky, A., Schlager, H., Scheibe, M., Diskin, G. S., DiGangi, J. P., Nowak, J. B., Zöger, M., and Borrmann, S.: Aircraft-based observation of meteoric material in lower-stratospheric aerosol particles between 15 and 68° N, Atmospheric Chemistry and Physics, 21, 989–1013, https://doi.org/10.5194/acp-21-989-2021, https://acp.copernicus.org/articles/21/989/2021/, 2021.

Schulz, C.: Secondary organic aerosol in the pristine Amazonian atmosphere: chemical properties, formation pathways, and interactions with clouds, Ph.D. thesis, Johannes Gutenberg-Universität Mainz, 2019.

Schulz, C., Schneider, J., Amorim Holanda, B., Appel, O., Costa, A., de Sá, S. S., Dreiling, V., Fütterer, D., Jurkat-Witschas, T., Klimach, T., Knote, C., Krämer, M., Martin, S. T., Mertes, S., Pöhlker, M. L., Sauer, D., Voigt, C., Walser, A., Weinzierl, B., Ziereis, H., Zöger, M., Andreae, M. O., Artaxo, P., Machado, L. A. T., Pöschl, U., Wendisch, M., and Borrmann, S.: Aircraft-based observations of isoprene-epoxydiol-derived secondary organic aerosol (IEPOX-SOA) in the tropical upper troposphere over the Amazon region, Atmospheric Chemistry and Physics, 18, 14 979–15 001, https://doi.org/10.5194/acp-18-14979-2018, https://acp.copernicus.org/articles/18/14979/2018/, 2018.

Siddiqui, S.: Studies of electrical properties of microchannel plates during and after high-temperature vacuum bakeout, IEEE Transactions on Electron Devices, 26, 1059–1064, https://doi.org/10.1109/T-ED.1979.19545, 1979.

Slater, D. C. and Timothy, J. G.: Microchannel plate modal gain variations with temperature, Review of Scientific Instruments, 64, 430–435, https://doi.org/10.1063/1.1144212, https://doi.org/10.1063/1.1144212, 1993.

Zanatta, M., Bozem, H., Köllner, F., Hoor, P., Schneider, J., Petzold, A., Bundke, U., Hayden, K., Staebler, R., Schulz, H., and Herber, A. B.: Airborne survey of trace gas and aerosol over the Southern Baltic Sea: from clean marine boundary layer to shipping corridor effect, submitted to Tellus B, 2019.

Ziegler, H.: Properties of Digital Smoothing Polynomial (DISPO) Filters, Appl. Spectrosc., 35, 88–92, http://www.osapublishing.org/as/abstract.cfm?URI=as-35-1-88, 1981.